Spectroscopic evidence for large aspherical β-NAT particles involved in denitrification in the December 2011 Arctic stratosphere

Wolfgang Woiwode[1], Michael Höpfner[1], Lei Bi[2,*], Michael C. Pitts[3], Lamont R. Poole[4], Hermann Oelhaf[1], Sergej Molleker[5], Stephan Borrmann[5,6], Marcus Klingebiel[6,**], Gennady Belyaev[7], Andreas Ebersoldt[8], Sabine Griessbach[9], Jens-Uwe Grooß[10], Thomas Gulde[1], Martina Krämer[10], Guido Maucher[1], Christof Piesch[1], Christian Rolf[10], Christian Sartorius[1], Reinhold Spang[10], Johannes Orphal[1]

[1]Institute of Meteorology and Climate Research, Karlsruhe Institute of Technology, Karlsruhe, Germany
[2]Department of Atmospheric Sciences, Texas A&M University, College Station, TX 77843, USA
[3]NASA Langley Research Center, Hampton, Virginia, 23681, USA
[4]Science Systems and Applications, Incorporated, Hampton, Virginia, 23666, USA
[5]Max Planck Institute for Chemistry, Particle Chemistry Department, Mainz, Germany
[6]Institute for Physics of the Atmosphere (IPA), University of Mainz, Mainz, Germany
[7]Myasishchev Design Bureau, Zhukovsky-5, Moscow Region, Russia
[8]Institute for Data Processing and Electronics, Karlsruhe Institute of Technology, Karlsruhe, Germany
[9]Jülich Supercomputing Centre (JSC), Forschungszentrum Jülich GmbH, 52425 Jülich, Germany
[10]Institute of Energy and Climate Research (IEK-7), Forschungszentrum Jülich GmbH, 52425 Jülich, Germany
*now at: School of Earth Sciences, Zhejiang University, Hangzhou, China, 310027
**now at: Max Planck Institute for Meteorology, Hamburg, Germany

Correspondence to: W. Woiwode (wolfgang.woiwode@kit.edu)

Abstract. We analyse polar stratospheric cloud (PSC) signatures in airborne MIPAS-STR (Michelson Interferometer for Passive Atmospheric Sounding – STRatospheric aircraft) observations under conditions suitable for the existence of nitric acid trihydrate (NAT) above northern Scandinavia on 11 December 2011. The high resolution infrared limb emission spectra of MIPAS-STR show a characteristic "shoulder-like" signature in the spectral region around 820 cm^{-1}, which is attributed to the ν_2 deformation mode of NO$_3^-$ in β-NAT. Using radiative transfer calculations involving Mie and T-Matrix methods, the spectral signatures of spherical and aspherical particles are simulated. The simulations are constrained using collocated in-situ particle measurements. Simulations assuming highly aspherical spheroids with aspect ratios (AR) of 0.1 or 10.0 and a lognormal particle mode with a mode radius of 4.8 µm reproduce the observed spectra to a high degree. A smaller lognormal mode with a mode radius of 2.0 µm, which was also taken into account, plays only a minor role. Best overall agreement is found for elongated spheroids with AR=0.1. Simulations of spherical particles and spheroids with AR=0.5 and 2.0 return results very similar to each other and do not allow to reproduce the signature around 820 cm^{-1}. The observed "shoulder-like" signature is explained by the combination of the emission and scattering characteristics of large highly aspherical β-NAT particles. The size distribution supported by our results corresponds with ~9 ppbv of gas-phase equivalent HNO$_3$ at the flight altitude of ~18.5 km. The results are compared with the size distributions derived from the in-situ observations, a corresponding Chemical Lagrangian Model of the Stratosphere (CLaMS) simulation, and excess gas-phase HNO$_3$ observed in a nitrification layer directly below the observed PSC. The presented results suggest that large highly aspherical β-NAT particles involved in denitrification of the polar stratosphere can be identified by means of passive infrared limb emission measurements.

1 Introduction

Nitric acid trihydrate (NAT) particles are known to be involved in denitrification and vertical downward transport of HNO_3 in the Arctic and Antarctic winter stratosphere and thereby affect polar ozone chemistry (e.g. Waibel et al., 1999; Carslaw et al., 2002.; Grooß et al., 2014). β-NAT is the only nitric acid hydrate known to be thermodynamically stable in condensed state under the conditions of the polar winter stratosphere (Tizek et al., 2004, and references therein). The presence of NAT in Arctic PSCs was confirmed by Voigt et al. (2000) using balloon-borne in-situ measurements of PSC particles. Large HNO_3-containing particles in Arctic PSCs likely consisting of NAT were also reported by Fahey et al. (2001).

Spang and Remedios (2003) and Spang et al. (2005) identified a "peak-like" signature in the spectral region around 820 cm^{-1} in spaceborne infrared PSC observations by CRISTA (Cryogenic Infrared Spectrometers and Telescopes for the Atmosphere) aboard the space shuttle and MIPAS (Michelson Interferometer for Passive Atmospheric Sounding) aboard Envisat. Based on Mie calculations, they suggested that the signature originated from the ν_2 band of the NO_3^{3-} in NAT particles with radii smaller than ~2-3 μm. Höpfner et al. (2006a) attributed the "peak-like" signature around 820 cm^{-1} in the MIPAS-Envisat PSC observations unambiguously to β-NAT by using a new set of refractive indices of β-NAT (Biermann, 1998) and explicit radiative transfer simulations for particles in limb-sounding observations (Höpfner et al., 2002). Particle radii lower than ~3 μm and volume densities higher than ~0.3 μm^3/cm^3 were derived.

Further in-situ observations of large potential NAT particles are reported by Brooks et al. (2003) and Molleker et al. (2014) and suggest extremely large particle sizes of 20 μm and more. Particle backward trajectories associated with in-situ observations of large potential NAT particles on 25 January 2010 suggest that the particles had experienced short growth times (Woiwode et al., 2014). However, the sizes of the largest particles derived from the in-situ observations are not reproduced by a state-of-the-art chemistry transport model parameterization (Hoyle et al., 2013; Grooß et al. 2014).

The metastable nitric acid dihydrate (NAD) is another constituent, which is likely present in PSCs and might be involved in the formation of NAT (Worsnop et al., 1993). Nucleation experiments in the cloud chamber AIDA (Aerosol, Interactions, and Dynamics in the Atmosphere) under stratospheric conditions resulted in formation of NAD, while no NAT formation was observed (Stetzer et al., 2006). While there is little evidence for nitric acid hydrates other than NAT in the stratosphere, Kim et al. (2006) reported observations of β-NAT along with NAD as a minor component in the Antarctic stratosphere by the ILAS-II instrument. However, a systematic search in MIPAS-Envisat spectra measured during the Antarctic winter 2003 showed no indication for any NAD particles with radii equal or less than about 1 μm (Höpfner et al., 2006a).

We use high resolution MIPAS-STR spectra and collocated in-situ observations during the high-altitude aircraft M-55 *Geophysica* (Stefanutti et al., 1999) ESSenCe (ESA Sounder Campaign 2011, Kaufmann et al., 2013) flight on 11 December 2011 inside an optically thin PSC to study the mid-infrared optical characteristics of large β-NAT particles in detail. The observations are brought into a synoptic context by comparisons with collocated observations by CALIPSO (Cloud-Aerosol Lidar and Infrared Pathfinder Satellite Observation, Pitts et al., 2011, 2013; Lambert et al., 2012, and references therein) and MIPAS-Envisat (Spang et al., 2005; Höpfner et al., 2006a, 2006b, and references therein).

Using radiative transfer simulations, we model the PSC signatures in the MIPAS-STR observations and constrain the simulations with collocated in-situ particle measurements. To simulate the signatures of spherical to highly aspherical β-NAT particles, we utilize the Mie code by Höpfner et al. (2002, 2006a) and the T-Matrix codes by Mishchenko and Travis (1998) and Bi et al. (2013). The assumption of highly aspherical β-NAT particles is supported by the work of Grothe et al. (2006),

5   who synthesized highly aspherical β-NAT particles under laboratory conditions.

In Sect. 2, we provide an overview on the meteorological situation, the MIPAS-STR and in-situ PSC observations during the *Geophysica* flight, and collocated CALIPSO and MIPAS-Envisat observations. In Sect. 3, we analyse the PSC signatures in the MIPAS-STR spectra using radiative transfer simulations. In Sect. 4, we compare the particle size distribution supported by the radiative transfer simulations with the size distributions derived from the in-situ observations, a Chemical Lagrangian

10 Model of the Stratosphere (CLaMS) simulation, and excess HNO_3 observed in a nitrification layer below the observed PSC. The results are summarized in Sect. 5.

2 PSC observations on 11 December 2011

2.1 Instrumentation

MIPAS-STR is a cryogenic Fourier transform spectrometer and provides high resolution limb emission spectra in the mid-

15 infrared (Piesch et al., 1996). Instrument characteristics, data processing, validation and PSC observations by MIPAS-STR are discussed by Woiwode et al. (2012, 2014, 2015). Here, we use MIPAS-STR channel 1 (725 to 990 cm^{-1}) and channel 2 (1150 to 1350 cm^{-1}) spectra recorded at a spectral sampling of 0.036 cm^{-1} and with an apodized spectral resolution of 0.069 cm^{-1} for cloud detection, retrievals of temperature and trace gases, and the analysis of PSC signatures. The apodized noise equivalent spectral radiance of the MIPAS-STR is typically ~$10 \cdot 10^{-9}$ W cm^{-2} sr^{-1} cm in channel 1 and ~$8 \cdot 10^{-9}$ W cm^{-2} sr^{-1} cm in channel

20 2. The vertical spacing of the utilized MIPAS-STR limb observations is mostly 1.0 km (1.5 km for lowest limb views) between ~5 km and flight altitude. Additional upward sampling provides limited information on the atmospheric scenario above (mainly column information). The horizontal along-track sampling during the discussed flight is ~33 km.

In-situ particle observations aboard the *Geophysica* were performed by the Forward Scattering Spectrometer Probe 100 (FSSP-100) and the Cloud Droplet Probe (CDP) (Molleker et al., 2014, and references therein). Both instruments detect

25 forward scattering of laser light at 633 nm (FSSP-100) and 658 nm (CDP). From the observations, particle size distributions in the ranges from 1.05 -37 μm (FSSP-100) and 4 -50 μm (CDP) are derived. The FSSP-100 and CDP measurements discussed here were evaluated using Mie theory, and particle sizes are indicated in diameter.

CALIOP (Cloud-Aerosol LIdar with Orthogonal Polarization) aboard the satellite CALIPSO is a two-wavelength polarization-sensitive lidar. CALIOP total and perpendicular backscatter coefficient observations at 532-nm are used for PSC identification

30 and classification according to Pitts et al. (2011, 2013). CALIPSO is part of the A-train constellation and provides observations up to 82° latitude in each hemisphere. The vertical and horizontal resolution of the PSC product are 180 m and 5 km, respectively.

MIPAS-Envisat is the spaceborne version of the MIPAS instruments (Fischer et al., 2008). Here, we use the spectral window from 780 to 860 cm^{-1} in channel A. The shown observations were performed in the reduced resolution nominal mode and have an apodized spectral resolution of 0.121 cm^{-1} (von Clarmann et al., 2009). The apodized noise equivalent spectral radiance of the MIPAS-Envisat channel A spectra is typically 11-19 W cm^{-2} sr^{-1} cm. Envisat was deployed on a polar orbit, with the

5   MIPAS-Envisat observations reaching up to ~89°N. The vertical and horizontal sampling of the observations discussed here were ~1.5 km and ~3.5° in latitude (~390 km), respectively.

2.2 Meteorological conditions, flight overview and PSC observations aboard the *Geophysica*

Figure 1 gives an overview of the meteorological situation and the observations from the *Geophysica* on 11 December 2011. The flight was performed between 11:05 and 15:00 UTC, with takeoff and landing in Kiruna, Sweden. Also shown are the

10   potential vorticity contours from the ECMWF (European Centre for Medium-Range Weather Forecasts) ERA-Interim reanalysis. The contours indicate that most of the flight was performed inside the polar vortex according to the criterion of Nash et al. (1996). The 430 K potential temperature level corresponds to a geometric altitude of ~18 km, which was the approximate flight altitude of the *Geophysica*. The flight was performed in a clock-wise pattern, and the polar vortex edge was crossed twice during the flight legs b and c.

15   Open black circles in Figure 1 indicate the tangent points of the MIPAS-STR limb observations. The horizontal distance of the tangent points from the flight path increases from a few tens of km to ~400 km with decreasing tangent altitude. The cloud index method by Spang et al. (2004) identifies cloud-affected MIPAS observations. In the case of MIPAS-Envisat, cloud index values higher than 4 are considered cloud-free, and values between 4 and 1 indicate the transition from slightly cloud-affected to opaque conditions. In Figure 1, MIPAS-STR observations with tangent altitudes >16 km (i.e. close to the flight track) and

20   cloud index values <3 are marked by filled circles. Here, we use a less conservative cloud index threshold of 3 to locate the PSC around the flight track north of ~68°N sharply. The flight section where the FSSP-100 and CDP detected the PSC (see Molleker et al., 2014) is indicated by the red line and coincides well with the MIPAS-STR PSC observations.

Figure 2 shows the vertical flight profile together with the MIPAS-STR tangent points colour-coded with the cloud index. After ascent, the *Geophysica* performed flight legs a and b at an approximately constant flight altitude of ~17 km. In leg c, an

25   approximately constant flight altitude of ~18 km was maintained until ~13:30 UTC. Finally, the *Geophysica* climbed to the ceiling altitude of ~18.5 km, until the descent phase was entered at ~14:20 UTC in leg e. From ~13:30 to 14:20 UTC, low cloud index values indicate the presence of a PSC around flight altitude. Particularly low cloud index values are found in the time interval where the in-situ instruments detected the PSC.

Several of the MIPAS-STR limb scans during the PSC encounter show low cloud index values from flight altitude towards

30   lower stratospheric altitudes. However, no sharp lower boundary of the PSC can be assigned, since the lower limb views are already affected by the PSC around flight altitude. At tropospheric altitudes, the cloud index values decrease towards 1 between 4 and 10 km and indicate tropospheric clouds.

2.3 CALIPSO PSC observations

Figure 3 shows the results of the closest-matching CALIPSO observations (see Fig. 1, 11:23 to 11:26 UTC). The observations were performed ~2 h prior to the *Geophysica* PSC encounter. The scattering ratio at 532 nm is the ratio of total volume backscatter to molecular backscatter and is sensitive to all types of cloud particles (Fig. 3a). The perpendicular backscatter coefficient at 532 nm is sensitive to depolarization of the backscattered light by aspherical cloud particles (Fig. 3b). The combination of inverse scattering ratio and the perpendicular backscatter at 532 nm is utilized for the CALIPSO PSC detection and classification according to Pitts et al. (2011, 2013) (Fig 3c). The method classifies mixtures dominated by STS (STS mix), mixtures of NAT and STS with increasing number densities of NAT (Mix1, Mix2 and Mix2-enh), ice-containing mixtures (Ice mix) and wave ice (Wave ice). Thereby, the utilization of the perpendicular backscatter at 532 nm enhances the detection of tenuous PSCs containing low number densities of NAT particles.

Usually, only CALIPSO nighttime observations are used for PSC detection and classification. Daytime CALIOP observations are characterized by strongly enhanced noise, making it much more difficult to detect enhanced backscatter from tenuous PSCs. In the case being discussed, strict exclusion of daytime observations would mean excluding CALIPSO observations south of 72.15°N and would greatly decrease the number of close-matching observations. To increase the number of close-matching CALIPSO observations, we included twilight observations down to 67°N. The comparison of the nighttime section >72.15°N and the twilight sections in the cross-sections in Figure 3 however provides a consistent picture of an extended PSC stretching from ~69°N northwards. False positive signal enhancements due to noise during twilight can be clearly distinguished as patchy spots at latitudes south of ~69°N.

In the vicinity of the *Geophysica* PSC observations, the scattering ratio and the perpendicular backscatter (Fig. 3a and 3b) faintly indicate a PSC between ~19 to 23 km. Between 69.0 and 71.4°N, the cluster of CALIPSO data with low scattering ratios and perpendicular backscatter values slightly exceeding the noise level suggest PSC layers consisting of NAT-containing mixtures (Fig. 3c). Much stronger signal enhancements and a more diverse composition are evident in the part of the PSC extending northward, which spans altitudes from ~18 to 25 km.

2.4 PSC signatures in airborne and spaceborne MIPAS observations

Figures 4a and 4b show the MIPAS-STR channel 1 and 2 spectra associated with the uppermost limb views of the limb scans during the time interval where the in-situ instruments detected the PSC (13:39 to 14:19 UTC). Within limb scans at the bottom of a PSC, the views in approximately horizontal geometry typically exhibit the strongest PSC signals. The observation at 13:47 UTC (black) belongs to the limb scan marked in magenta in Figures 1 and 2. A cloud-free observation at 12:27 UTC (grey) is shown for comparison. Compared to the cloud-free observation, the PSC spectra show a strong continuum-like offset of typically 150 to 300 · 10^{-9} W cm^{-2} sr^{-1} cm in channel 1 (Fig. 4a). The continuum-like offset results from upwelling greybody-like emission from the surface and/or tropospheric clouds, which is scattered by the PSC particles. A characteristic "shoulder-like" signature is found in the spectral region around 820 cm^{-1}, which is shaded in light cyan here and in the following.

The channel 2 spectra (Fig 4b) are characterized by lower overall radiances when compared to channel 1. The spectra show a characteristic continuum-like offset of up to ~100 · 10^{-9} W cm^{-2} sr^{-1} cm at the lower boundary of the channel, which decreases towards higher wavenumbers. Absorption signatures of gaseous H_2O are found between 1170 and 1250 cm^{-1} (blue arrows in Fig. 4b) and are the consequence of absorption of upwelling broad-band radiation from the surface and/or low clouds by the abundant H_2O molecules in the lower troposphere (see Höpfner et al., 2002).

Figure 5 shows a spectral window from 780 to 860 cm^{-1} of MIPAS-Envisat channel A observations in the vicinity of the *Geophysica* flight exhibiting PSC signatures (from visual inspection) (see Fig. 1). The observations with tangent altitudes close to the *Geophysica* flight altitude also show a "shoulder-like" signature in the spectral region around 820 cm^{-1} similar to the MIPAS-STR observations.

2.5 Ambient conditions and indications for PSC composition

Figure 6 shows the vertical cross-sections of temperature and $HNO_{3(g)}$ retrieved from the MIPAS-STR observations. In Appendix A (Fig. 17) we furthermore show the associated vertical cross-sections of $H_2O_{(g)}$ and O_3, since these results are used below. Where applicable, the physical state of HNO_3 and H_2O is indicated by "(g)" for "gaseous" and "(s)" for "solid". All other discussed compounds are gaseous under stratospheric conditions, and the physical state is not indicated explicitly.

The vertical cross-section of temperature in Figure 6a typically shows temperatures above 200 K around flight altitude until ~13:00 UTC. From the second half of section c to section e and in particular during the PSC encounter, lower temperatures between 195-200 K are found above 16 km. The observed temperatures are close to typical values of T_{NAT} (Hanson and Mauersberger, 1988) and above the existence temperatures of STS (T_{STS}, ~3.5 K below T_{NAT}, Drdla et al., 2003) and ice (T_{ice}, ~7 K below T_{NAT}, Murphy and Koop, 2005).

The vertical cross-section of $HNO_{3(g)}$ shows mixing ratios increasing with altitude in general (Fig. 6b). In horizontal direction, the mixing ratios around and below flight altitude slightly decrease in section b and increase again at the beginning of section c, indicating the crossing of the vortex edge (compare Fig. 1). Between 13:15 and 14:15 UTC, a local $HNO_{3(g)}$ maximum peaking at ~16 km is observed. The maximum is located below the PSC encounter of the *Geophysica* (see Sect. 2.1) and extends into the PSC observed at flight altitude. In contrast, the vertical cross-section of the stratospheric tracer O_3 in Appendix A (Fig. 17) shows no corresponding maximum, suggesting that the $HNO_{3(g)}$ maximum originated from nitrification. In Figure 7, we show T_{NAT} calculated from the MIPAS-STR $HNO_{3(g)}$ and $H_2O_{(g)}$ observations during the PSC encounter. T_{NAT} is calculated using the thermodynamic relationships of Hanson and Mauersberger (1988). The T_{NAT} profiles are compared with the corresponding temperature profiles derived from the MIPAS-STR observations, the *Geophysica* UCSE (Unit for Connection with Scientific Equipment) onboard temperature sensor measurements, radiosonde temperature profiles from Bodø and Bjornoya (12Z launches, see Fig. 1) and ECMWF temperature profiles (here: ECMWF T106 grid-point analysis). The same ECMWF profiles served as the initial guess and a priori profiles for the MIPAS-STR temperature retrievals.

The MIPAS-STR $HNO_{3(g)}$ and $H_2O_{(g)}$ profiles used for the calculation of T_{NAT} are shown in Appendix A (Fig 18). The $H_2O_{(g)}$ profiles are furthermore compared with in-situ observations of total H_2O by FISH (Fast In-situ Stratospheric Hygrometer; Zöger et al., 1999; Meyer et al., 2015) during the same flight for quality assessment.

During the PSC encounter, both MIPAS-STR and the *Geophysica* UCSE in-situ temperature sensor indicate temperatures
5   between 192-200 K around flight altitude. The UCSE temperatures are slightly lower than the temperatures measured by MIPAS-STR. Both observations are consistent with the radiosonde profiles from Bodø (south of PSC encounter) and Bjornoya (north of PSC encounter). The ECMWF temperatures are in close agreement with the UCSE data. Slightly higher and more variable temperatures are derived from MIPAS-STR around flight altitude and hint at enhanced uncertainties (e.g. additional errors due to a weak cloud index threshold of 2 applied in the retrievals) and/or horizontal temperature variations around the
10   flight track.

While several MIPAS-STR temperature profiles approach T_{NAT} values already at altitudes >16 km, the UCSE in-situ and ECMWF temperatures approach T_{NAT} at ~18 km. The same T_{NAT} profiles were also calculated considering offsets of (i) +20% in both $HNO_{3(g)}$ and $H_2O_{(g)}$ and (ii) -20 % in both $HNO_{3(g)}$ and $H_2O_{(g)}$ (i.e. offsets for $HNO_{3(g)}$ and $H_2O_{(g)}$ acting into the same direction in terms of T_{NAT}). The offset T_{NAT} profiles indicate a weak sensitivity of T_{NAT} to uncertainties in $HNO_{3(g)}$ and $H_2O_{(g)}$.
15   The close agreement of the temperatures measured by MIPAS-STR, the UCSE data and the ECMWF data with calculated T_{NAT} around flight altitude suggests that the observed PSC was composed of β-NAT. NAD is another possible candidate due to similar formation and persistence conditions when compared with β-NAT (Worsnop et al., 1993; Tizek et al., 2004). STS and ice are unlikely candidates due to too high temperatures.

To investigate the accumulated vertical HNO_3 redistribution at the locations of the flight, the correlations of the MIPAS-STR
20   $HNO_{3(g)}$ and O_3 profiles associated with the PSC encounter (see Fig. 18a and 18c) and profiles outside the polar vortex are shown in Figure 8. O_3 is well suited as stratospheric tracer in this case, since the altitude range under consideration is hardly affected by Arctic winter depletion at this early stage of the polar winter. Maximum differences in $HNO_{3(g)}$ of ~5 ppbv are found between the data points associated with the PSC encounter and the data points outside the vortex for O_3 mixing ratios around 1.6 to 1.8 ppmv. For the profiles associated with the PSC encounter, this coincides with the altitude range of the
25   observed nitrification maximum peaking at ~16 km (Fig. 6b).

3 Analysis of PSC signatures in the MIPAS-STR spectra

3.1 Radiative transfer model and simulation scenario

To simulate the MIPAS-STR spectra, we use the Karlsruhe Optimized and Precise Radiative Transfer Algorithm (KOPRA, Stiller et al., 2002). KOPRA is a fast line-by-line code and allows the modelling of infrared limb observations, including trace
30   gas signatures, cloud parameters and instrumental characteristics. Modelling of MIPAS PSC observations using a Mie model and based on single scattering is discussed and validated by Höpfner et al. (2002, 2006a), Höpfner (2004) and Höpfner and Emde (2004), respectively. In the following, we consider the MIPAS-STR limb view at 13:47 UTC in approximately horizontal

orientation (black spectra in Fig. 4a and 4b), which was performed well within the PSC and shows developed PSC signatures. Table 1 provides an overview of the radiative transfer scenarios discussed in the following. For simulating the signatures of β-NAT, we use the "NATcoa" refractive indices by Biermann (1998), which have been applied successfully for the identification for small β-NAT particles by Höpfner et al. (2006a, 2006b). The signatures of NAD are simulated using the

5 refractive indices by Niedzela et al. (1998). For simulating STS, we use the refractive indices by Biermann et al. (2000) for 45 wt% solutions of HNO_3/H_2O, since these compounds are expected to dominate the optical properties of STS (Höpfner et al., 2006a). For ice, we use the refractive indices by Zasetsky et al. (2005) for 200 K.

Particle size distributions are assumed lognormal in shape and characterized by the mode radii (r), geometric standard deviations (i.e. mode width, σ) and mode number densities (N). For simplification, we assume that these quantities are constant

10 over the entire vertical range covered by the PSC. We constrain the used size distributions with the FSSP-100 and CDP in-situ observations during the same flight. In Figure 9a, the particle size distributions derived by Molleker et al. (2014) from the FSSP-100 and CDP observations (black and magenta, respectively) during the PSC encounter are shown. Figure 9b shows the lognormal size distributions used in the radiative transfer simulations of the MIPAS-STR observations (for parameters see Table 2). The bimodal size distribution A (Fig. 9b, red) resembles approximately the size distribution derived from the

15 FSSP-100 observations.

To improve the agreement of the simulated spectra with the measurements, only the mode radii of size distribution A are scaled. Accordingly, the particle number densities and mode widths are maintained, while the particle sizes and thereby the volume of $HNO_{3(s)}$ are scaled. In Figure 9b, size distribution B corresponds with the size distribution resulting in the best agreement of the radiative transfer simulations with the MIPAS-STR observations (see below). Size distribution B is obtained

20 from size distribution A by scaling the radii of both modes by a factor of 0.8. Scenarios B1 and B2 are sensitivity calculations with respect to the importance of the larger mode and a hypothetic small particle mode with enhanced number density.

For modelling of aspherical particles, spheroids are assumed. The aspect ratio (AR) is the ratio of the horizontal and rotational semi-axis. Elongated spheroids are characterized by AR < 1, and oblate spheroids by AR > 1. For easy comparisons, the sizes of aspherical particles are given in r or D of volume-equivalent spherical particles.

25 In the simulations, we adopt a vertical PSC extent from 17-23 km altitude, which is supported by the MIPAS-STR and CALIPSO observations (see Sect. 2.2 and 2.3). The tropospheric cloud scenario is defined considering the MIPAS-STR cloud index values of the associated limb scan. Further information on the tropospheric cloud scenario is inferred from the fact that tropospheric $H_2O_{(g)}$ absorption signatures are identified in the MIPAS-STR spectra (see Fig. 4b). While the MIPAS-STR cloud index values suggest a tropospheric cloud top slightly below 10 km (see Fig. 2), the presence of the $H_2O_{(g)}$ absorption lines

30 requires partially transparent conditions down to low tropospheric altitudes (Höpfner et al., 2002). Both criteria are fulfilled by assuming a partially transparent tropospheric cloud from 0 to 10 km characterized by a low continuum extinction coefficient α of 0.0223 km^{-1} (i.e. ~98 % transmission per 1 km-layer), providing efficient transmission of radiation from nadir directions and increasing opaqueness towards limb geometry at altitudes covered by the tropospheric clouds. Note however that this is a simplified assumption for a probably much more complex and horizontally variable cloud scenario in the reality.

A sea surface temperature of ~280.2 K is adopted as surface temperature from the NOAA Optimum Interpolation (OI) SST V2 GraDS image of the flight day (see http://www.esrl.noaa.gov/psd/) in combination with a sea surface emissivity of 0.99 (see Newman et al., 2005).

Vertical profiles of trace gases required for the simulations of the spectra are retrieved previously from the full cloud-filtered MIPAS-STR limb scans. The retrievals of temperature (utilizing CO_2 signatures), O_3, $HNO_{3(g)}$, $ClONO_2$, CFC-11, and CFC-12 are performed according to Woiwode et al. (2012, 2015). $H_2O_{(g)}$, N_2O, CH_4, COF_2, CFC-22 and CCl_4 are retrieved from the MIPAS-STR channel 1 and 2 spectra in specific microwindows using the same strategy. As the MIPAS-STR limb observations provide only information above the tropospheric cloud top, the profiles are extrapolated to lower altitudes based on the slopes of the a priori profiles. The profiles of temperature and the strong tropospheric absorber $H_2O_{(g)}$ below the tropospheric cloud top are constructed from the radiosonde observations from Bodø and Bjornoya (see Fig. 1). For CO_2, the corresponding polar winter profile for MIPAS of Remedios et al. (2007) is updated for the polar winter 2011/12. For the minor constituents SF_6, CFC-14 and N_2O_5, the polar winter profiles from Remedios et al. (2007) are adopted.

3.2 Mie calculations of spherical β-NAT, NAD, STS and ice particles

For simulations of the ensemble-averaged single scattering parameters of spherical β-NAT, NAD, STS and ice particles, we use the Mie model coupled to KOPRA (Höpfner et al., 2002, 2006a; Höpfner, 2004). The Mie model provides the wavenumber-dependent ensemble-averaged phase functions, extinction cross-sections and single scattering albedos required for the simulation of the scattering and absorption/emission of radiation by the particles.

Figure 10 shows the results of the Mie calculations based on size distributions A and B. The upper panels show the simulated spectra together with the observed MIPAS-STR channel 1 and 2 spectra. The residuals between simulation and observation are shown in the lower panels. For size distribution A, the Mie calculations of β-NAT show systematically higher radiances in channel 1 by typically about 50 to 100·10^{-9} W cm^{-2} sr^{-1} cm when compared to the measurement (Fig. 10a and 10b, red). The residual values decrease towards the lower and upper boundary of the channel. A characteristic dip is found in the spectral region around 820 cm^{-1}, where the "shoulder-like" signature is located in the observations.

Enhanced "line-like" residuals in the densely populated spectral regions below 810 cm^{-1} (mostly CO_2 and O_3), between 850 to 920 cm^{-1} ($HNO_{3(g)}$), as well as above 970 cm^{-1} (O_3), are explained by uncertainties in the knowledge of the profiles of the corresponding trace gases at tropospheric altitudes and above the flight path. The uncertainties of these parts of the profiles are translated into the simulated spectra by to the simulated scattering of radiation by the particles from outside into field-of-view. Further sources of uncertainties are limitations in the simulated scattering scenario (e.g. limited number of scattering angles). Furthermore, the noise equivalent spectral radiance of the MIPAS-STR spectra steeply increases towards the channel boundaries and enhances the variability in the residuals in these regions.

In channel 2, the simulated radiances are systematically lower by ~25·10^{-9} W cm^{-2} sr^{-1} below 1300 cm^{-1} and show better agreement with the measurements at higher wavenumbers for size distribution A. Similar to the observation, prominent $H_2O_{(g)}$ absorption signatures are found between 1170 and 1250 cm^{-1} in the simulation (indicated black arrows in Fig. 10 to Fig. 12).

Further "line-like" residuals exceeding the noise level are again explained by uncertainties in the knowledge of the profiles of the corresponding trace gases at tropospheric altitudes and above the flight path (here mostly O_3, N_2O, CH_4 and HNO_3), limitations in the simulated scattering scenario and increasing noise towards the channel boundaries.

The results for size distribution B (Fig. 10a and 10b, blue) show improved agreement in channel 1. However, a dip is observed again in the spectral region around 820 cm^{-1}, and the residual values are increasingly negative towards the lower and upper boundary of channel 1. In channel 2, the residual values below 1300 cm^{-1} are more negative when compared to size distribution A.

For NAD (Fig. 10c and 10d), similar residuals are found for both size distributions when compared to β-NAT. The residual signatures in the spectral region around 820 cm^{-1} in channel 1 have a more "step-like" shape. For STS (Fig. 10e and 10f), again similar residuals are found when compared to β-NAT, including a dip in the spectral region around 820 cm^{-1} for both size distributions. When compared with the previous cases, the simulation of STS using size distribution A results in the best agreement with the observations in channel 2 (Fig. 10f, red).

For ice (Fig. 10g and 10h), the worst overall agreement is found in channel 1. For both size distributions, the simulated spectrum shows a negative overall gradient from the lower to the upper boundary of the channel. Negative residual values as low as -200·10^{-9} W cm^{-2} sr^{-1} cm are found at the upper end of channel 1 for both size distributions, and again a dip is found in the spectral region around 820 cm^{-1}. In channel 2, the observed radiances are slightly overestimated below ~1250 cm^{-1} for size distribution A and significantly underestimated below 1300 cm^{-1} for size distribution B.

Overall, the results of the Mie simulations show worse agreement with the observations and prominent residual signatures in the spectral region around 820 cm^{-1}. In the following simulations of aspheric particles, we exclude NAD, STS and ice as dominating constituents of the observed PSC for the following reasons:

- β-NAT is the only candidate exhibiting a characteristic spectral signature around 820 cm^{-1} and the only PSC constituent known to be thermodynamically stable under the conditions of the flight.

- While NAD shows a similar spectral signature centred at 808 cm^{-1} (Niedziela et al., 1998) when compared with β-NAT, the signature is not capable of reproducing the residual dip slightly below 820 cm^{-1} (see Sect. 3.5). Furthermore, the observations indicate temperatures close to the threshold temperature of β-NAT (i.e. slightly too warm for NAD) and suggest large aged particles. Therefore, a transformation of potential previous metastable NAD particles into thermodynamically stable β-NAT appears likely.

- STS droplets are not expected to grow to the large sizes observed in-situ and are not supported by the observed temperatures (e.g. Peter, 1998). Furthermore, STS droplets are expected to be approximately spherical. However, the presented Mie calculations for spherical STS droplets result only in coarse agreement with the observations.

- For ice, the observed temperatures are considerably too warm, and the Mie calculations result in the worst overall agreement.

3.3 T-Matrix calculations of β-NAT particles with moderate aspect ratios

For simulations of the ensemble-averaged single scattering parameters of moderately aspherical β-NAT particles, we use the double-precision T-Matrix code for polydisperse, randomly oriented, rotationally symmetric particles by Mishchenko and Travis (1998). The T-Matrix is calculated according to the extended boundary condition method (EBCM) (Waterman, 1971).

5 Advantages of this code are fast computations for moderately aspherical particles and the capability of direct coupling to KOPRA. The same setup as in the Mie calculations is used.

The results for elongated spheroids with AR=0.5 and oblate spheroids with AR=2.0 are shown in Figure 11. Briefly, the results for both AR values are very similar to each other and to the Mie scenario (compare Fig. 10a and b) for both size distributions. Again, a characteristic dip is found in the spectral region around 820 cm^{-1} for both AR values and size distributions.

3.4 T-Matrix calculations of β-NAT particles with extreme aspect ratios

For simulations of the ensemble-averaged single scattering parameters of highly aspherical β-NAT particles, we use invariant imbedding and separation of variables (IIM+SOV) T-Matrix calculations (Bi et al., 2013). Again, polydisperse, randomly oriented spheroids and the same setup as in the previous scenarios are considered. To allow flexible variation of size distributions and save computing time, the optical parameters of β-NAT particles are calculated for discrete wavenumbers ν

15 (Δν=1 cm^{-1}) and sizes (r=0.5 to 20 μm with Δr=0.5 μm) and are tabulated. Particle size distributions are implemented by means of binned lognormal size distributions referring to the tabulated optical parameters.

The results of the simulations with AR=0.1 and AR=10.0 are shown in Figure 12. For AR=0.1 and size distribution A, high systematic offsets of 100 to 200·10^{-9} W cm^{-2} sr cm are found in channel 1 and up to ~50·10^{-9} W cm^{-2} sr cm in channel 2 (Fig. 12a and 12b, red). In contrast, size distribution B results in a much flatter residual pattern close to zero in wide ranges of

20 channel 1 and in the entire channel 2 (Fig. 12a and 12b, blue). For both AR values and size distributions, the residual peak in the spectral region around 820 cm^{-1} flattens out to a high degree in contrast to the previous simulations. The H$_2$O$_{(g)}$ absorption signatures in the spectral range from 1170 to 1250 cm^{-1} are reproduced well for size distribution B.

For AR=10.0 and size distribution A, again high residual values of typically around 100 to 150·10^{-9} W cm^{-2} sr cm are found in channel 1 and mostly below 50·10^{-9} W cm^{-2} sr cm in channel 2 (Fig. 12c and 12d, red), whereas size distribution B results in

25 improved agreement with the observation (Fig. 12c and 12d, blue). When compared to the corresponding AR=0.1 scenario, increasingly negative residual values are found towards the upper boundary of channel 1, and slightly negative residual values below 1300 cm^{-1} in channel 2. However, the spectral region around 820 cm^{-1} in channel 1 is reproduced slightly better than in the AR=0.1 case.

Both scenarios, elongated spheroids with AR=0.1 and oblate spheroids with AR=10.0 result in considerably improved

30 agreement with the observations when compared with the previous simulations. For both size distributions, the residual dip in the spectral region around 820 cm^{-1} flattens out significantly.

For size distribution B, the spectral range above 900 cm^{-1} is furthermore reproduced well by the AR=0.1 scenario, and good agreement is found in channel 2. As in the previous cases, residual patterns remain especially in the densely populated spectral regions and at the channel boundaries.

3.5 Sensitivity to aspect ratio and comparison with refractive indices

5 In the following, we compare the radiative transfer simulations of elongated spheroids consisting of β-NAT with different aspect ratios. The same comparison for oblate spheroids results in similar conclusions. Figures 13a and 13b show the results of the Mie scenario (AR=1.0, cyan) and the T-Matrix calculations with AR=0.5 (magenta) and AR=0.1 (green) for size distribution B.

The scenarios with AR=1.0 and 0.5 show only small differences of a few 10^{-9} W cm^{-2} sr^{-1} cm. For AR=0.5, the residual peak

10 in the spectral region around 820 cm^{-1} decreases slightly, and the spectrum is tilted slightly towards the observation in the higher wavenumber region of channel 1. Slightly improved agreement with the observation is found also in channel 2. In contrast, the agreement with the observation is improved considerably for AR=0.1: in channel 1, the residual dip in the spectral region around 820 cm^{-1} flattens out to a high degree. The simulated spectrum is tilted towards the observation above 900 cm^{-1} and reproduces the observed spectrum in this region well. In channel 2, higher radiances in close agreement with the

15 observation are found when compared to the other scenarios.

Figure 13c and 13d show the imaginary parts of the refractive indices of β-NAT, NAD, STS and ice, which determine the emission and absorption characteristics of the particles. In the spectral region around 820 cm^{-1}, which is weakly populated by trace gas signatures, β-NAT is the only candidate exhibiting a mode capable of contributing to the observed residual signature. Figures 13e and 13f show the real parts of the refractive indices of the discussed species, which determine the scattering of

20 radiation from outside into the field-of-view. Again, β-NAT is the only candidate showing a characteristic "step-like" signature in the spectral region around 820 cm^{-1}, which is capable of contributing to the observed signature. The combination of the "peak-like" emission signature (determined by the refractive index imaginary part) and the "step-like" scattering signature (determined by the refractive index real part) of β-NAT provides the prerequisite to reproduce the observed "shoulder-like" net signature for highly aspherical particles.

25 NAD also shows a similar "peak-like" signature at ~808 cm^{-1} in the refractive index imaginary part and a "step-like" signature below ~810 cm^{-1} with weaker amplitudes when compared with β-NAT. Therefore, potential highly aspheric large NAD particles are expected to produce a similar "shoulder-like" signature below 810 cm^{-1} with weaker amplitude.

The relative contributions of emission and scattering to the observed signature is investigated in Figure 14 for the AR=1.0 scenario (magenta) and the AR=0.1 (green) scenario. Also shown are the same simulations neglecting the scattering by the

30 particles (violet and dark green, respectively). Thereby, the wavenumber-dependent ensemble-averaged particle extinction coefficients are calculated taking into account only the emission/absorption by the particles and neglecting the scattering source function.

For AR=0.1, the scenario neglecting scattering by the particles results in lower radiances by up to ~200·10^{-9} W cm^{-2} sr^{-1} cm in channel 1 (Fig. 14a) and ~100·10^{-9} W cm^{-2} sr^{-1} cm in channel 2 (Fig. 14b) when compared to the same scenario including scattering. This demonstrates the importance of the scattering source function. The same effect is found to a lesser degree also in the corresponding AR=1.0 scenarios. The AR=1.0 and the AR=0.1 scenarios neglecting scattering show only small differences in the order of 10·10^{-9} W cm^{-2} sr^{-1} cm from each other. Enhanced differences of ~30·10^{-9} W cm^{-2} sr^{-1} cm are however found in the spectral region around 820 cm^{-1}, where a weak "peak-like" signature with a maximum at ~817 cm^{-1} can be identified in the AR=0.1 scenario due to emission by the 820 cm^{-1} mode of β-NAT.

Much higher discrepancies between the AR=1.0 and AR=0.1 scenario are seen if scattering is included, and a "shoulder-like" net signature peaking at ~814 cm^{-1} is found in the AR=0.1 scenario. In the observations, the shoulder-like signature is more narrow than in the simulation and peaks at ~818 cm^{-1}. The simulation represents the increasing flank from higher towards lower radiances very well, while the maximum and the decreasing flank towards lower radiances are located at lower wavenumbers and are broader than in the simulation.

We point out that there are still remaining systematic discrepancies between the simulation of β-NAT for AR=0.1 and the observation. Beside the limitations of the radiative transfer simulation and scenario, the discrepancies are attributed to uncertainties in the refractive indices used (30% uncertainty for imaginary parts, see Höpfner et al., 2006a; not quantified for real parts) and the fact that the refractive indices are only available at a spectral resolution of 1 cm^{-1}. In contrast, the MIPAS-STR observations have a considerably higher apodized resolution of 0.068 cm^{-1}. Another reason for the observed discrepancies might be the simplified particle shape assumed in the simulations. Real β-NAT particles might have different and more complex shapes and are likely to have edges and flat surfaces, altering their optical characteristics.

3.6 Sensitivity calculations on tropospheric scenario for β-NAT, AR=0.1

In the following, we investigate the sensitivity of the AR=0.1 scenario for β-NAT and size distribution B on modifications of the tropospheric cloud scenario and sea surface temperature. Figure 15 shows this scenario (Fig. 15a-15d, green, hereafter "optimized scenario") together with sensitivity simulations considering modified tropospheric cloud scenarios (see Table 1). The optimized scenario uses a tropospheric cloud layer between 0 and 10 km characterized by a continuum absorption coefficient of 0.0223 km^{-1} (at all wavelengths) and a sea surface temperature of 280.2 K (see Sect. 3.1).

The first modified tropospheric cloud scenario considering an opaque tropospheric cloud from 0 to 2 km and fully transparent conditions above hardly changes the simulated spectra in both channels when compared to the optimized scenario (Fig 15a and 15b, magenta). This modified scenario is motivated by CALIPSO observations of tropospheric clouds during the scan from 11:23 to 11:26 (not shown, see http://www-calipso.larc.nasa.gov/products/), indicating a dense cloud layer below ~2 km. Note however that CALIPSO provides vertical cross-sections corresponding with a narrow footprint and that the horizontal cloud distribution is variable. The second modified scenario neglects the presence of any tropospheric clouds (Fig. 15a and 15b, cyan). The comparison with the optimized scenario and the observation shows that the radiances in both channels are significantly overestimated. However, a "shoulder-like" signature in the spectral region around 820 cm^{-1} can be identified.

The third modified scenario considers the extreme case of an opaque tropospheric cloud between 0 to 10 km (Fig. 15c and 15d, cyan). High negative offsets are found in both channels when compared to the observation, and the $H_2O_{(g)}$ absorption signatures between 1170 and 1250 cm^{-1} are not reproduced. Accordingly, this scenario confirms the requirement for partially transparent conditions down to low tropospheric altitudes. However, also this scenario weakly indicates a "shoulder-like"

5   signature around 820 cm^{-1}. Finally, the scenario with a 7 K lower surface temperature (i.e. 273.2 K, Figs 15c and 15d, magenta) results only in small changes when compared to the optimized scenario. Accordingly, the identification of the "shoulder-like" signature around 820 cm^{-1} is robust against the adopted tropospheric cloud and tropospheric radiation emission scenario. The presence of partially transparent conditions down to the low troposphere is confirmed.

3.7 Sensitivity calculations on PSC scenario for β-NAT, AR=0.1

10   In the following, the sensitivity of the simulated spectra to the thickness of the simulated PSC layer and the adopted particle size distribution is investigated. Figure 16 shows the optimized AR=0.1 scenario (green) using size distribution B together with sensitivity simulations considering a reduced PSC top altitude and modified size distributions (see Fig. 9b and Tables 1 and 2). The scenario with a lower PSC top altitude of 20 km instead of 23 km shows a significant negative offset in both channels (Fig. 16a and 16b, orange). Both, the signature around 820 cm^{-1} in channel 1 and the $H_2O_{(g)}$ absorption signatures in

15   channel 2 show smaller amplitudes when compared to the optimized scenario.

The scenario considering only the second mode of the size distribution B (size distribution B1, see Fig. 9b and Table 2) results only in small changes when compared to the optimized scenario (Fig. 16a and 16b, cyan). Accordingly, the first mode of size distribution B is of minor importance for the simulated radiances. We furthermore investigate the role of a hypothetic mode of small β-NAT particles with a high number density, which might have been present above the flight path and contributed to the

20   observed spectra. In size distribution B2 (see Fig. 9b and Table 2), the first mode is replaced by a small particle mode with a mode radius of 0.5 μm and a number density enhanced by a factor of 100. The corresponding total amount of condensed $HNO_{3(g)}$ is comparable with size distribution B (see Table 3). The resulting simulated spectra (Fig. 16a and 16b, magenta) are almost identical to the optimized scenario. Accordingly, the exact shape of the first mode is if minor importance, as long as the amount of condensed $HNO_{3(g)}$ is maintained.

25   So in summary, reducing the simulated PSC layer thickness by 50 % results in significantly lower simulated radiances. However, the overall spectral pattern, a weak signature around 820 cm^{-1} and $H_2O_{(g)}$ absorption signatures between 1170 and 1250 cm^{-1} can be identified. Omitting the first mode of particle size distribution B or replacing the first mode by a small particle mode with similar HNO_3-content result only in small changes in the simulated spectra. Accordingly, the identification of the β-NAT signature around 820 cm^{-1} is robust against the assumed thickness of the PSC layer and modifications of the size

30   distribution in the considered ranges. The second mode of size distribution B with a mode radius of 4.8 μm plays the key role in the simulation of the overall offset due to scattering and the "shoulder-like" signature around 820 cm^{-1}.

4 Comparison of simulated and observed particle size distributions

In the following, we compare the amounts of gas-phase equivalent HNO_3 corresponding with size distributions A, B, B1 and B2 with the same quantity derived from the in-situ observations by the FSSP-100 and CDP (see Tables 2 and 3 and Fig. 9). Gas-phase equivalent HNO_3 is calculated for pressure and temperature at flight altitude. The results are furthermore compared

5   with a corresponding size distribution simulated by the CLaMS for the area from 70.0°N to 72.0°N and 15.0°E to 22.5°E in the altitude range from ~18.0 to 18.5 km at 14:00 UTC (Fig. 9b). Finally, the results are compared with excess $HNO_{3(g)}$ in the nitrification layer below the flight path retrieved from the MIPAS-STR measurements.

The bimodal size distribution A corresponds with 18.2 ppbv gas-phase equivalent HNO_3 and resembles approximately the size distribution derived from the FSSP-100 observations, which corresponds to 18.5 ppbv of gas-phase equivalent HNO_3. The

10   optimized size distribution B and size distributions B1 and B2 correspond to gas-phase equivalent HNO_3 from 8.4 to 9.8 ppbv. Size distribution B was derived from size distribution A by reducing the mode radii of both modes by 20 %. The corresponding large difference in condensed HNO_3 is the consequence of the high sensitivity of particle volume on particle radius.

The CLaMS size distribution shown in Figure 9b includes an STS mode (below 3 μm in the shown range of dN/dlog(D)) and a binned NAT mode. While the small STS mode hardly contributes to the total amount of condensed HNO_3 in the simulation,

15   the NAT mode contains a considerably smaller amount of gas-phase equivalent HNO_3 of only ~1.6 ppbv when compared to size distribution B and more than one order of magnitude less gas-phase equivalent HNO_3 than derived from the in situ observations. In the CLaMS simulation, a more narrow NAT mode results, peaking at the size bin centred at r=3.7 μm. The largest particles are found in the size bin centred at r=4.7 μm.

While the occurrence of PSCs and overall denitrification are reproduced well by CLaMS in general (Grooß et al., 2014), the

20   discrepancy between the size distribution simulated by CLaMS and derived from the observations discussed here might by linked to uncertainties in the simulated NAT nucleation rates, missing nucleation processes (e.g. NAT nucleation on pre-existing ice) and simulated particle growth rates.

Furthermore, sedimentation rates for spherical particles are assumed in the CLaMS simulations. However, aspherical particles, such as supported by the observations discussed here, would have lower sedimentation rates than spherical NAT particles,

25   which affects the time-dependent development of particle size distributions inside PSCs and HNO_3 redistribution in general (Woiwode et al., 2014). Furthermore, locations and altitudes of specific PSCs and atmospheric structures in model simulations and observations can differ from each other, while the overall processes are represented in a realistic way in the model simulations.

The maximum amount of excess $HNO_{3(g)}$ of ~5 ppbv in the nitrification layer below the flight track (see Fig. 8) is used as an

30   estimate for the amount of condensed excess HNO_3 in the observed PSC layer around flight altitude. Since the particles observed at flight altitude have sizes of mostly considerably larger than 1 μm and such particles are characterized by significant sedimentation rates, the associated amount of condensed HNO_3 is most likely excess HNO_3 originating from higher altitudes.

Converting the amount of excess HNO_3 present at ~16 km to the conditions at the flight altitude of ~18.5 km results in a mixing ratio of ~7.5 ppbv, which is comparable with gas-phase equivalent HNO_3 derived from size distributions B, B1 and B2. Accordingly, the size distributions B, B1 and B2 supported by the simulations of the MIPAS-STR spectra suggest by factors of ~2 to 3 smaller amounts of condensed HNO_3 when compared to the size distributions derived from the in-situ observations.

5 The CLaMS simulation suggests a smaller amount of condensed HNO_3 by a factor of ~6 when compared with size distribution B and by more than one order of magnitude less condensed HNO_3 when compared with the size distributions derived from the in-situ observations. While the origin of the observed nitrification around 16 km is not necessarily linked to the PSC observed above, the associated amount of excess $HNO_{3(g)}$ supports that the amounts of gas-phase equivalent HNO_3 associated with size distributions B, B1 and B2 are realistic.

10 5 Conclusions

The MIPAS-STR observations associated with the Arctic PSC flight on 11 December 2011 show a characteristic "shoulder-like" signature in the spectral region around 820 cm^{-1}, which is attributed to the ν_2 deformation mode of NO_3^- of β-NAT. The observed signature is explained by the emission and scattering characteristics of large highly aspheric β-NAT particles. While Mie calculations and T-Matrix calculations assuming spheroids with moderate AR values of 0.5 and 2.0 do not reproduce the

15 observed signature and the overall spectral patterns, T-Matrix calculations for spheroids involving extreme AR values of 0.1 and 10.0 result in reasonable agreement with the observations. In the discussed scenario, best agreement is found for AR=0.1 and a bimodal lognormal size distribution with mode radii of 2.0 and 4.8 μm when adopting a particle size distribution similar in shape with the results from the collocated in-situ observations. The smaller mode with a mode radius of 2.0 μm plays only a minor role in the simulations.

20 The combination of the MIPAS-STR cloud, temperature and trace gas data products, collocated in-situ observations aboard the *Geophysica*, CALIPSO observations and radiosonde observations allow us to define the radiative transfer scenario accurately. The scattering of upwelling tropospheric radiation by the particles plays an important role in the simulation of the overall spectral patterns and in particular of the "shoulder-like" signature around 820 cm^{-1}. The importance of scattering is also reflected by the observation of prominent $H_2O_{(g)}$ absorption signatures in the MIPAS-STR limb emission spectra between

25 1170 to 1250 cm^{-1}, implying scattering of radiation from the low troposphere/surface into the field-of-view. Remaining discrepancies between the radiative transfer simulations and the observations are attributed to the limitations of the radiative transfer simulation and scenario, the uncertainties and the comparably coarse spectral resolution of the available refractive index data, and the uncertain particle geometries.

The radiative transfer simulations of the MIPAS-STR observations suggest ~20 % smaller radii when compared to the size

30 distributions derived from the in-situ observations, resulting in factors of 2-3 smaller amounts of condensed β-NAT. A corresponding CLaMS simulation suggests a factor of ~6 less condensed HNO_3 and smaller particles when compared to the radiative transfer simulations. This discrepancy might be linked to uncertainties and limitations of the NAT nucleation, particle

growth and particle sedimentation rates (which would be different for highly aspherical particles) simulated by CLaMS and the limited comparison with the localised case study being discussed. Excess $HNO_{3(g)}$ derived from the MIPAS-STR observations in the nitrification layer below the observed PSC shows that the amounts of condensed HNO_3 supported by the radiative transfer simulations are realistic.

5 The larger particle sizes derived from the FSSP-100 and CDP measurements after evaluation using the Mie theory are not necessarily in contradiction with the radiative transfer simulations of the MIPAS-STR observations discussed here when interpreted as maximum dimensions of highly aspherical particles. For example, elongated spheroids with extreme aspect ratios can easily span lengths of several tens of microns while having relatively small individual particle volumes. Evidence of particles with sizes of this magnitude is provided by CIP shadow cast images recorded during the Arctic winter 2009/10
10 (Molleker et al. 2014).

The results of our radiative transfer calculations suggest smaller volumes of individual particles than suggested by non-optical measurements during other PSC flights (Fahey et al., 2001; Molleker et al., 2014). However, the particle sizes derived here suggest significant sedimentation rates and associated vertical redistribution of HNO_3. We mention that the shapes of particle size distributions of PSCs depend on the specific growing conditions of the particles. Furthermore, there might be some
15 diversity in the NAT phase in terms of particle sizes and shapes, which is not captured by the assumption of lognormal size distributions and a single particle geometry. Real stratospheric β-NAT particles might have more complex shapes similar to ice (e.g. Libbrecht, 2005), and hollow NAT shells were proposed as an alternative explanation for large particle sizes derived from in-situ measurements (Molleker et al., 2014; see also Biermann et al., 1998).

The shapes and sizes of large β-NAT particles are important parameters for simulations of denitrification, chemistry and
20 radiation in the polar stratosphere and for the interpretation of infrared limb observations, in-situ particle measurements and lidar observations. The presented results show that large highly aspherical β-NAT particles show a characteristic spectral signature, which may be exploited for the identification of large β-NAT particles involved in denitrification. Further laboratory measurements of the refractive indices of β-NAT particles with high spectral resolution would help to improve radiative transfer simulations and retrievals from high resolution mid-infrared limb observations. The application of the T-Matrix
25 method for highly aspherical particle shapes would help in the interpretation of in-situ forward scattering measurements of β-NAT particles (compare Borrmann et al., 2000). Further airborne remote sensing and in-situ PSC observations in the Arctic stratosphere using the combination of optical and non-optical methods would help to better characterize β-NAT particles, and advanced in-situ measurements would allow actual measurement of the particle shapes (e.g. Kaye et al., 2008).

Appendix A

30 The vertical cross-sections of $H_2O_{(g)}$ and O_3 retrieved from the MIPAS-STR observations are shown in Figure 17. In the O_3 cross-section (Fig. 17b), the mixing ratios around and below flight altitude decrease in section b and increase again at the beginning of section c similar to HNO_3 (see Fig. 6b) and indicate the crossing of the vortex edge (see Fig. 1).

The absence of a local O_3 maximum between 13:15 and 14:15 UTC around ~16 km confirms that the $HNO_{3(g)}$ maximum in Figure 6b is the result of a nitrification process. The vertical profiles of $HNO_{3(g)}$, H_2O and O_3 used for the calculation of T_{NAT} and the O_3-$HNO_{3(g)}$ correlation in Section 2.5 are shown in Figure 18.

Acknowledgements

5   The authors thank Myasishchev Design Bureau and the ESSenCe coordination team for a successful *Geophysica* field campaign. ESSenCe was supported by the European Space Agency/Mission Science Division under the ESSenCe project (Technical Assistance for the Deployment of Airborne Limbsounders during ESSenCe). W. Woiwode is grateful to the Karlsruhe House for Young Scientists for supporting a 5-month research stay at NASA Langley airborne Research Center (NASA LaRC, Hampton, USA), and thanks M. Pitts and L. Poole from the CALIPSO PSC team for a great and productive

10 time at NASA LaRC. We thank M. I. Mishchenko (NASA Goddard Institute for Space Studies, New York, USA) for helpful recommendations and providing the contact to L. Bi (Department of Atmospheric Sciences, Texas A&M University, College Station, USA, now at: School of Earth Sciences, Zhejiang University, Hangzhou, China), who performed the extensive IIM+SOV T-Matrix calculations. For calculations for moderately aspheric particles, we used the double-precision T-Matrix code for randomly oriented nonspherical particles provided by M. I. Mishchenko, L. D. Travis, and D. W. Mackowski at

15 http://www.giss.nasa.gov/staff/mmishchenko/t_matrix.html. The dataset for the simulation of highly aspherical β-NAT particles used here is available by L. Bi (bilei@zju.edu.cn). We thank U. M. Biermann, R. F. Niedziela and A. Y. Zasetsky for providing the refractive indices of β-NAT, STS, NAD and ice. The CLaMS simulation was performed using computing time granted on the supercomputer JUROPA at Jülich Supercomputing Centre (JSC) under the VSR project ID JICG11. We thank EMCWF for the data used for the MIPAS-STR retrievals, the CLaMS simulation and the potential vorticity map. We thank

20 Wyoming Atmospheric Soundings (Department of Atmospheric Science, University of Wyoming, USA) for providing the radiosonde data (see http://weather.uwyo.edu/upperair/sounding.html). We acknowledge the Physical Sciences Division, Earth System Research Laboratory, NOAA, Boulder, Colorado, USA, for providing the sea surface temperature data (see http://www.esrl.noaa.gov/psd/). We thank R. Müller (Institute of Energy and Climate Research (IEK-7), Forschungszentrum Jülich GmbH, Germany) for helpful comments. We acknowledge support by the Deutsche Forschungsgemeinschaft and Open

25 Access Publishing Fund of the Karlsruhe Institute of Technology.

References

Bi, L., Yang, P., Kattawar, G. W., and Mishchenko, M. I.: Efficient implementation of the invariant imbedding T-matrix method and the separation of variables method applied to large nonspherical inhomogeneous particles, J. Quant. Spectrosc. Radiat. Transfer, 116, 169-183, 2013.

Biermann, U. M.: Gefrier- und FTIR-Experimente zur Nukleation und Lebensdauer stratosphärischer Wolken, Ph.D. thesis, Universität Bielefeld, cuvillier Verlag, ISBN 3-89712-212-X, 1998.

Biermann, U. M., Crowley, J. N., Huthwelker, T., Moortgat, G. K., Crutzen, P. J., and Peter, T.: FTIR studies on lifetime prolongation of stratospheric ice particles due to NAT coating, Geophys. Res. Lett., 25, 3939–3942, doi:10.1029/1998GL900040, 1998.

Biermann, U. M., Luo, B. P., and Peter, T.: Absorption spectra and optical constants of binary and ternary solutions of H_2SO_4, HNO_3, and H_2O in the mid infrared at atmospheric temperatures, J. Phys. Chem. (A), 104, 783–793, 2000.

Borrmann, S., Luo, B., and Mishchenko, M.: The application of the T-matrix method to the measurement of aspherical particles with forward scattering optical particle counters, J. Aerosol Sci., 31, 789–799, 2000.

Brooks, S. D., Baumgardner, D., Gandrud, B., Dye, J. E., Northway, M. J., Fahey, D. W., Bui, T. P., Toon, O. B., and Tolbert, M. A.: Measurements of large stratospheric particles in the Arctic polar vortex, J. Geophys. Res., 108, 4652, doi:10.1029/2002JD003278, 2003.

Carslaw, K. S., Kettleborough, J. A., Northway, M. J., Davies, S., Gao, R., Fahey, D. W., Baumgardner, D. G., Chipperfield, M. P., and Kleinböhl, A.: A vortex-scale simulation of the growth and sedimentation of large nitric acid hydrate particles, J. Geophys. Res., 107, 8300, doi:10.1029/2001JD000467, 2002.

Drdla, K., Gandrud, B. W., Baumgardner, D., Wilson, J. C., Bui, T. P., Hurst, D., Schauffler, S. M., Jost, H., Greenblatt, J. B., and Webster, C. R.: Evidence for the widespread presence of liquid-phase particles during the 1999–2000 Arctic winter, J. Geophys. Res., 108, 8318, doi:10.1029/2001JD001127, 2003.

Fahey, D. W., Gao, R. S., Carslaw, K. S., Kettleborough, J., Popp, P. J., Northway, M. J., Holecek, J. C., Ciciora, S. C., McLaughlin, R. J., Thompson, T. L., Winkler, R. H., Baumgardner, D. G., Gandrud, B., Wennberg, P. O., Dhaniyala, S., McKinley, K., Peter, T., Salawitch, R. J., Bui, T. P., Elkins, J. W., Webster, C. R., Atlas, E. L., Jost, H., Wilson, J. C., Herman, R. L., Kleinböhl, A., and von König, M.: The detection of large HNO_3-containing particles in the winter Arctic stratosphere, Science, 291, 1026–1031, 2001.

Fischer, H., Birk, M., Blom, C., Carli, B., Carlotti, M., von Clarmann, T., Delbouille, L., Dudhia, A., Ehhalt, D., Endemann, M., Flaud, J. M., Gessner, R., Kleinert, A., Koopman, R., Langen, J., López-Puertas, M., Mosner, P., Nett, H., Oelhaf, H., Perron, G., Remedios, J., Ridolfi, M., Stiller, G., and Zander, R.: MIPAS: an instrument for atmospheric and climate research, Atmos. Chem. Phys., 8, 2151-2188, doi:10.5194/acp-8-2151-2008, 2008.

Grooß, J.-U., Engel, I., Borrmann, S., Frey, W., Günther, G., Hoyle, C. R., Kivi, R., Luo, B. P., Molleker, S., Peter, T., Pitts, M. C., Schlager, H., Stiller, G., Vömel, H., Walker, K. A., and Müller, R.: Nitric acid trihydrate nucleation and denitrification in the Arctic stratosphere, Atmos. Chem. Phys., 14, 1055-1073, doi:10.5194/acp-14-1055-2014, 2014.

Grothe, H., Tizek, H., Waller, D., and Stokes, D. J.: The crystallization kinetics and morphology of nitric acid trihydrate, Phys. Chem. Chem. Phys., 8, 2232–2239, doi:10.1039/B601514J, 2006.

Hanson, D. and Mauersberger, K.: Laboratory studies of the nitric acid trihydrate: implications for the south polar stratosphere, Geophys. Res. Lett., 15, 855–858, doi:10.1029/GL015i008p00855, 1988.

Höpfner, M., Oelfhaf, H., Wetzel, G., et al.: Evidence of scattering of tropospheric radiation by PSCs in mid-IR emission spectra: MIPAS-B observations and KOPRA simulations, Geophys. Res. Lett., 29(8), doi:10.1029/2001GL014443, 2002.

Höpfner, M.: Study on the impact of polar stratospheric clouds on high resolution mid–IR limb emission spectra, J. Quant. Spectrosc. Radiat. Transfer, 83, 93–107, 2004.

Höpfner, M. and Emde, C.: Comparison of single and multiple scattering approaches for the simulation of limb–emission observations in the mid–IR, J. Quant. Spectrosc. Radiat. Transfer, 91, 275–285, 2004.

Höpfner, M., Luo, B. P., Massoli, P., Cairo, F., Spang, R., Snels, M., Di Donfrancesco, G., Stiller, G., von Clarmann, T., Fischer, H., and Biermann, U.: Spectroscopic evidence for NAT, STS, and ice in MIPAS infrared limb emission measurements of polar stratospheric clouds, Atmos. Chem. Phys., 6, 1201-1219, doi:10.5194/acp-6-1201-2006, 2006a.

Höpfner, M., Larsen, N., Spang, R., Luo, B. P., Ma, J., Svendsen, S. H., Eckermann, S. D., Knudsen, B., Massoli, P., Cairo, F., Stiller, G., v. Clarmann, T., and Fischer, H.: MIPAS detects Antarctic stratospheric belt of NAT PSCs caused by mountain waves, Atmos. Chem. Phys., 6, 1221-1230, doi:10.5194/acp-6-1221-2006, 2006b.

Hoyle, C. R., Engel, I., Luo, B. P., Pitts, M. C., Poole, L. R., Grooß, J.-U., and Peter, T.: Heterogeneous formation of polar stratospheric clouds – Part 1: Nucleation of nitric acid trihydrate (NAT), Atmos. Chem. Phys., 13, 9577-9595, doi:10.5194/acp-13-9577-2013, 2013.

Kaufmann, M., Blank, J., Friedl-Vallon, F., Gerber, D., Guggenmoser, T., Höpfner, M., Kleinert, A., Sha, M. K., Oelhaf, H., Riese, M., Suminska-Ebersoldt, O., Woiwode, W., Siddans, R., Kerridge, B., Moyna, B., Rea, S., and Oldfield, M.: Technical Assistance for the Deployment of Airborne Limbsounders during ESSenCe, Tech. rep., European Space Agency, 2013.

Kaye, P., Hirst, E., Greenaway, R., Ulanowski, Z., Hesse, E., DeMott, P., Saunders, C., and Connolly, P.: Classifying atmospheric ice crystals by spatial light scattering, Opt. Lett., 33, 1545-1547, doi:10.1364/OL.33.001545, 2008.

Kim, Y., Choi, W., Lee, K., Park, J. H., Massie, S. T., Sasano, Y., Nakajima, H., and Yokota, T.: Polar stratospheric clouds observed by the ILAS-II in the Antarctic region: Dual compositions and variation of compositions during June to August of 2003, J. Geophys. Res., 111, D13S90, doi:10.1029/2005JD006445, 2006.

Lambert, A., Santee, M. L., Wu, D. L., and Chae, J. H.: A-train CALIOP and MLS observations of early winter Antarctic polar stratospheric clouds and nitric acid in 2008, Atmos. Chem. Phys., 12, 2899-2931, doi:10.5194/acp-12-2899-2012, 2012.

Libbrecht, K. G.: The physics of snow crystals., Rep. Prog. Phys., 68, 855–895, 2005.

Meyer, J., Rolf, C., Schiller, C., Rohs, S., Spelten, N., Afchine, A., Zöger, M., Sitnikov, N., Thornberry, T. D., Rollins, A. W., Bozóki, Z., Tátrai, D., Ebert, V., Kühnreich, B., Mackrodt, P., Möhler, O., Saathoff, H., Rosenlof, K. H., and Krämer, M.: Two decades of water vapor measurements with the FISH fluorescence hygrometer: a review, Atmos. Chem. Phys., 15, 8521-8538, doi:10.5194/acp-15-8521-2015, 2015.

Mishchenko, M. I. and Travis, L. D.: Capabilities and limitations of a current FORTRAN implementation of the T-matrix method for randomly oriented rotationally symmetric scatterers, J. Quant. Spectrosc. Radiat. Transfer, 60, 309–324, 1998.

Molleker, S., Borrmann, S., Schlager, H., Luo, B., Frey, W., Klingebiel, M., Weigel, R., Ebert, M., Mitev, V., Matthey, R., Woiwode, W., Oelhaf, H., Dörnbrack, A., Stratmann, G., Grooß, J.-U., Günther, G., Vogel, B., Müller, R., Krämer, M.,

Meyer, J., and Cairo, F.: Microphysical properties of synoptic-scale polar stratospheric clouds: in-situ measurements of unexpectedly large HNO_3 containing particles in the Arctic vortex, Atmos. Chem. Phys., 14, 10785-10801, doi:10.5194/acp-14-10785-2014, 2014.

Murphy, D. M. and Koop, T.: Review of the vapour pressures of ice and supercooled water for atmospheric applications, Q. J. Roy. Meteor. Soc., 131, 1539–1565, 2005.

Nash, E. R., Newman, P. A., Rosenfield, J. E., and Schoeberl, M. R.: An objective determination of the polar vortex using Ertel's potential vorticity, J. Geophys. Res., 101, 9471–9478, 1996.

Newman, S. M., Smith, J. A., Glew, M. D., Rogers, S. M., and Taylor, J. P.: Temperature and salinity dependence of sea surface emissivity in the thermal infrared, Q. J. Roy. Meteorol. Soc., 131, 2539–2557, 2005.

Niedziela, R. F., Miller, R. E., and Worsnop, D. R.: Temperature and frequency-dependent optical constants for nitric acid dehydrate from aerosol spectroscopy, J. Phys. Chem. (A), 102, 6477-6484, 1998.

Peter, T.: Microphysics and Heterogeneous Chemistry of Polar Stratospheric Clouds, Annu. Rev. Phys. Chem., 48, 785–822, doi:10.1146/annurev.physchem.48.1.785, 1997.

Piesch, C., Gulde, T., Sartorius, C., Friedl-Vallon, F., Seefeldner, M., Wölfel, M., Blom, C. E., and Fischer, H.: Design of a MIPAS instrument for high-altitude aircraft, Proc. of the 2nd Internat. Airborne Remote Sensing Conference and Exhibition, ERIM, Ann Arbor, MI, Vol. II, 199-208, 1996.

Pitts, M. C., Poole, L. R., Dörnbrack, A., and Thomason, L. W.: The 2009–2010 Arctic polar stratospheric cloud season: a CALIPSO perspective, Atmos. Chem. Phys., 11, 2161-2177, doi:10.5194/acp-11-2161-2011, 2011.

Pitts, M. C., Poole, L. R., Lambert, A., and Thomason, L. W.: An assessment of CALIOP polar stratospheric cloud composition classification, Atmos. Chem. Phys., 13, 2975-2988, doi:10.5194/acp-13-2975-2013, 2013.

Remedios, J. J., Leigh, R. J., Waterfall, A. M., Moore, D. P., Sembhi, H., Parkes, I., Greenhough, J., Chipperfield, M.P., and Hauglustaine, D.: MIPAS reference atmospheres and comparisons to V4.61/V4.62 MIPAS level 2 geophysical data sets, Atmos. Chem. Phys. Discuss., 7, 9973–10017, doi:10.5194/acpd-7-9973-2007, 2007.

Spang, R. and Remedios, J. J.: Observations of a distinctive infrared spectral feature in the atmospheric spectra of polar stratospheric clouds measured by the CRISTA instrument, Geophys. Res. Lett., 30(16), 1875, doi:10.1029/2003GL017231, 2003.

Spang, R., Remedios, J. J., and Barkley, M. P.: Colour indices for the detection and differentiation of cloud types in infra-red limb emission spectra, Adv. Space Res., 33, 1041–1047, 2004.

Spang, R., Remedios, J. J., Kramer, L. J., Poole, L. R., Fromm, M. D., Müller, M., Baumgarten, G., and Konopka, P.: Polar stratospheric cloud observations by MIPAS on ENVISAT: detection method, validation and analysis of the northern hemisphere winter 2002/2003, Atmos. Chem. Phys., 5, 679-692, doi:10.5194/acp-5-679-2005, 2005.

Stefanutti, L., Sokolov, L., Balestri, S., MacKenzie, A. R., and Khattatov, V.: The M-55 Geophysica as a platform for the airborne polar experiment, J. Atmos. Ocean. Tech., 16, 1303–1312, doi:10.1175/1520-0426(1999)016<1303:tmgaap>2.0.co;2, 1999.

Stetzer, O., Möhler, O., Wagner, R., Benz, S., Saathoff, H., Bunz, H., and Indris, O.: Homogeneous nucleation rates of nitric acid dihydrate (NAD) at simulated stratospheric conditions – Part I: Experimental results, Atmos. Chem. Phys., 6, 3023-3033, doi:10.5194/acp-6-3023-2006, 2006.

Stiller, G. P., von Clarmann, T., Funke, B., Glatthor, N., Hase, F., Höpfner, M., and Linden, A.: Sensitivity of trace gas abundances retrievals from infrared limb emission spectra to simplifying approximations in radiative transfer modelling, J. Quant. Spectrosc. Radiat. Transfer, 72, 249–280, doi:10.1016/S0022-4073(01)00123-6, 2002.

Tizek, H., Knözinger, E. and Grothe, H.: Formation and phase distribution of nitric acid hydrates in the mole fraction range x_{HNO3}<0.25: A combined XRD and IR study, Phys. Chem. Chem. Phys., 6, 972-979, doi:10.1039/B310672A, 2004.

Voigt, C., Schreiner, J., Kohlmann, A., Zink, P., Mauersberger, K., Larsen, N., Deshler, T., Kröger, C., Rosen, J., Adriani, A., Cairo, F., Di Donfrancesco, G., Viterbini, M., Ovarlez, J., Ovarlez, H., David, C., and Dörnbrack, A.: Nitric Acid Trihydrate (NAT) in Polar Stratospheric Clouds, Science, 290, 1756–1758, 2000.

von Clarmann, T., Höpfner, M., Kellmann, S., Linden, A., Chauhan, S., Funke, B., Grabowski, U., Glatthor, N., Kiefer, M., Schieferdecker, T., Stiller, G. P., and Versick, S.: Retrieval of temperature, H_2O, O_3, HNO_3, CH_4, N_2O, $ClONO_2$ and ClO from MIPAS reduced resolution nominal mode limb emission measurements, Atmos. Meas. Tech., 2, 159-175, doi:10.5194/amt-2-159-2009, 2009.

Waibel, A. E., Peter, Th., Carslaw, K. S., Oelhaf, H., Wetzel, G., Crutzen, P. J., Pöschl, U., Reimer, E., and Fischer, H.: Arctic ozone loss due to denitrification, Science, 283, 2064–2069, 1999.

Waterman, P.: Symmetry, unitarity, and geometry in electromagnetic scattering, Phys. Rev., 3, 825–839, 1971.

Woiwode, W., Oelhaf, H., Gulde, T., Piesch, C., Maucher, G., Ebersoldt, A., Keim, C., Höpfner, M., Khaykin, S., Ravegnani, F., Ulanovsky, A. E., Volk, C. M., Hösen, E., Dörnbrack, A., Ungermann, J., Kalicinsky, C., and Orphal, J.: MIPAS-STR measurements in the Arctic UTLS in winter/spring 2010: instrument characterization, retrieval and validation, Atmos. Meas. Tech., 5, 1205-1228, doi:10.5194/amt-5-1205-2012, 2012.

Woiwode, W., Grooß, J.-U., Oelhaf, H., Molleker, S., Borrmann, S., Ebersoldt, A., Frey, W., Gulde, T., Khaykin, S., Maucher, G., Piesch, C., and Orphal, J.: Denitrification by large NAT particles: the impact of reduced settling velocities and hints on particle characteristics, Atmos. Chem. Phys., 14, 11525-11544, doi:10.5194/acp-14-11525-2014, 2014.

Woiwode, W., Sumińska-Ebersoldt, O., Oelhaf, H., Höpfner, M., Belyaev, G. V., Ebersoldt, A., Friedl-Vallon, F., Grooß, J.-U., Gulde, T., Kaufmann, M., Kleinert, A., Krämer, M., Kretschmer, E., Kulessa, T., Maucher, G., Neubert, T., Piesch, C., Preusse, P., Riese, M., Rongen, H., Sartorius, C., Schardt, G., Schönfeld, A., Schuettemeyer, D., Sha, M. K., Stroh, F., Ungermann, J., Volk, C. M., and Orphal, J.: Validation of first chemistry mode retrieval results from the new limb-imaging FTS GLORIA with correlative MIPAS-STR observations, Atmos. Meas. Tech., 8, 2509-2520, doi:10.5194/amt-8-2509-2015, 2015.

Worsnop, D. R., Zahniser, M. S., Fox, L. E., and Wofsy, S. C.: Vapor Pressures of Solid Hydrates of Nitric Acid: implications for Polar Stratospheric Clouds, Science, 259, 71–74, 1993.

Zasetsky, A. Y., Khalizov, A. F., Earle, M. E., and Sloan, J. J.: Frequency Dependent Complex Refractive Indices of Supercooled Liquid Water and Ice Determined from Aerosol Extinction Spectra, J. Phys. Chem. A, 109, 2760–2764, 2005.

Zöger, M., Afchine, A., Eicke, N., Gerhards, M. T., Klein, E., McKenna, D. S., Morschel, U., Schmidt, U., Tan, V., Tuitjer, F., Woyke, T., and Schiller, C.: Fast in-situ stratospheric hygrometers: a new family of balloon-borne and airborne Lyman

5   alpha photofragment fluorescence hygrometers, J. Geophys. Res., 104, 1807–1816, 1999.

Table 1. Overview of radiative transfer scenarios.

ID	Species	Size distribution	Code / aspect ratio (AR)	Vertical PSC extent [km]	Vertical range of trop. cloud [km] / α [km^{-1}]	Comment
43	β-NAT	B	Mie[a] / 1.0	17-23	0-10 / 0.0223	
43a	β-NAT	B	Mie[a] / 1.0	17-23	0-10 / 0.0223	no scattering
44	β-NAT	A	Mie[a] / 1.0	17-23	0-10 / 0.0223	
45	STS	B	Mie[a] / 1.0	17-23	0-10 / 0.0223	
46	STS	A	Mie[a] / 1.0	17-23	0-10 / 0.0223	
47	NAD	B	Mie[a] / 1.0	17-23	0-10 / 0.0223	
48	NAD	A	Mie[a] / 1.0	17-23	0-10 / 0.0223	
51	Ice	B	Mie[a] / 1.0	17-23	0-10 / 0.0223	
52	Ice	A	Mie[a] / 1.0	17-23	0-10 / 0.0223	
53	β-NAT	B	TM[b] / 0.5	17-23	0-10 / 0.0223	
54	β-NAT	A	TM[b] / 0.5	17-23	0-10 / 0.0223	
55	β-NAT	B	TM[b] / 2.0	17-23	0-10 / 0.0223	
56	β-NAT	A	TM[b] / 2.0	17-23	0-10 / 0.0223	
57	β-NAT	B	TM[c] / 0.1	17-23	0-10 / 0.0223	
57a	β-NAT	B	TM[c] / 0.1	17-23	0-10 / 0.0223	no scattering
57b	β-NAT	B	TM[c] / 0.1	17-23	0-2 / 5.000	
57c	β-NAT	B	TM[c] / 0.1	17-23	. /.	
57d	β-NAT	B	TM[c] / 0.1	17-23	0-10 / 5.000	
57e	β-NAT	B	TM[c] / 0.1	17-23	0-10 / 0.0223	$T_{Surface}$ = 273.2 K
57f	β-NAT	B	TM[c] / 0.1	17-20	0-10 / 0.0223	
57g	β-NAT	B1	TM[c] / 0.1	17-23	0-10 / 0.0223	
57i	β-NAT	B2	TM[c] / 0.1	17-23	0-10 / 0.0223	
58	β-NAT	A	TM[c] / 0.1	17-23	0-10 / 0.0223	
59	β-NAT	B	TM[c] / 10.0	17-23	0-10 / 0.0223	
60	β-NAT	A	TM[c] / 10.0	17-23	0-10 / 0.0223	

[a]Mie code, Höpfner et al. (2006a)

[b]EBCM T-Matrix code, Mishchenko and Travis (1998)

[c]IIM+SOV T-Matrix code, Bi et al. (2013)

Table 2. Particle size distributions used in radiative transfer scenarios.

Size distribution	Mode 1			Mode 2		
	r_1 [µm]	σ_1	N_1 [cm^{-3}]	r_2 [µm]	σ_2	N_2 [cm^{-3}]
A	2.5	1.5	$1.6 \cdot 10^{-3}$	6.0	1.35	$1.5 \cdot 10^{-3}$
B	2.0	1.5	$1.6 \cdot 10^{-3}$	4.8	1.35	$1.5 \cdot 10^{-3}$
B1	./.	./.	./.	4.8	1.35	$1.5 \cdot 10^{-3}$
B2	0.5	1.5	$1.6 \cdot 10^{-1}$	4.8	1.35	$1.5 \cdot 10^{-3}$

10   Table 3. Comparison of equivalent $HNO_{3(g)}$ corresponding with the particle size distributions used in the radiative transfer simulations of the MIPAS-STR observations, the size distributions derived from the in-situ measurements, and a CLaMS simulation, together with excess $HNO_{3(g)}$ derived for the nitrification layer below the observed PSC.

Size Distribution	$HNO_{3(g)}$ [ppbv]	Comment
A	18.2	radiative transfer simulation, starting point
B	9.3	radiative transfer simulation, optimized scenario
B1	8.4	radiative transfer simulation, sensitivity
B2	9.8	radiative transfer simulation, sensitivity
FSSP-100	18.5	derived from in-situ observation
CDP	28.5	derived from in-situ observation
CLaMS	1.6	chemistry transport simulation
nitrification layer[a]	5.0	excess $HNO_{3(g)}$ @ ~16.0 km
	7.5	equivalent $HNO_{3(g)}$ @ 18.5 km

[a]see Sect. 2.5
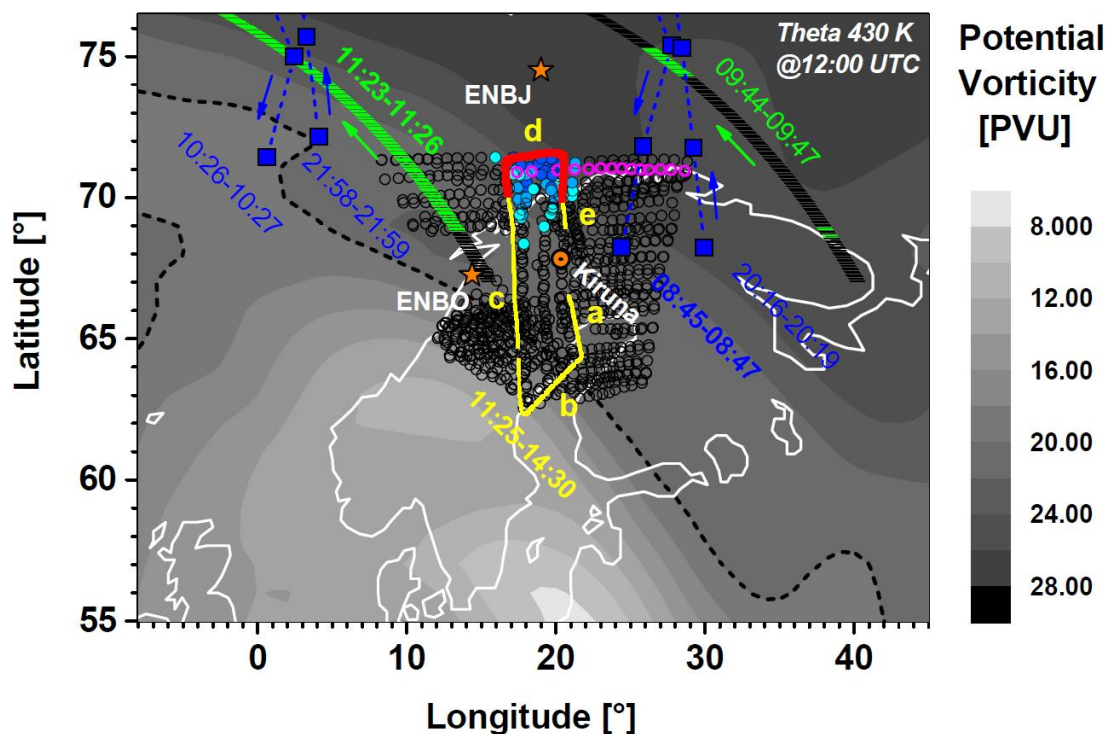
Figure 1. Flight path (yellow line) of the *Geophysica* and meteorological situation during the PSC flight on 11 December 2011. Grey shading: ECMWF ERA-Interim potential vorticity at the potential temperature level of 430 K. Black dashed line: polar vortex edge according to Nash et al. (1996). Open black circles: MIPAS-STR tangent points. Filled circles (cyan to blue): MIPAS-STR tangent points >16 km with cloud index <3. Magenta circles: MIPAS-STR limb scan associated with spectra considered in radiative transfer simulations. Red line: flight section of FSSP-100 and CDP PSC observations. Horizontal green/black bars: CALIPSO PSC observations (green: PSC detected at 21 km). Filled blue squares: MIPAS-Envisat observations at 18.4 to 19.0 km exhibiting PSC signatures. Orange stars: radiosonde launch sites Bodø (ENBO) and Bjornoya (ENBJ).
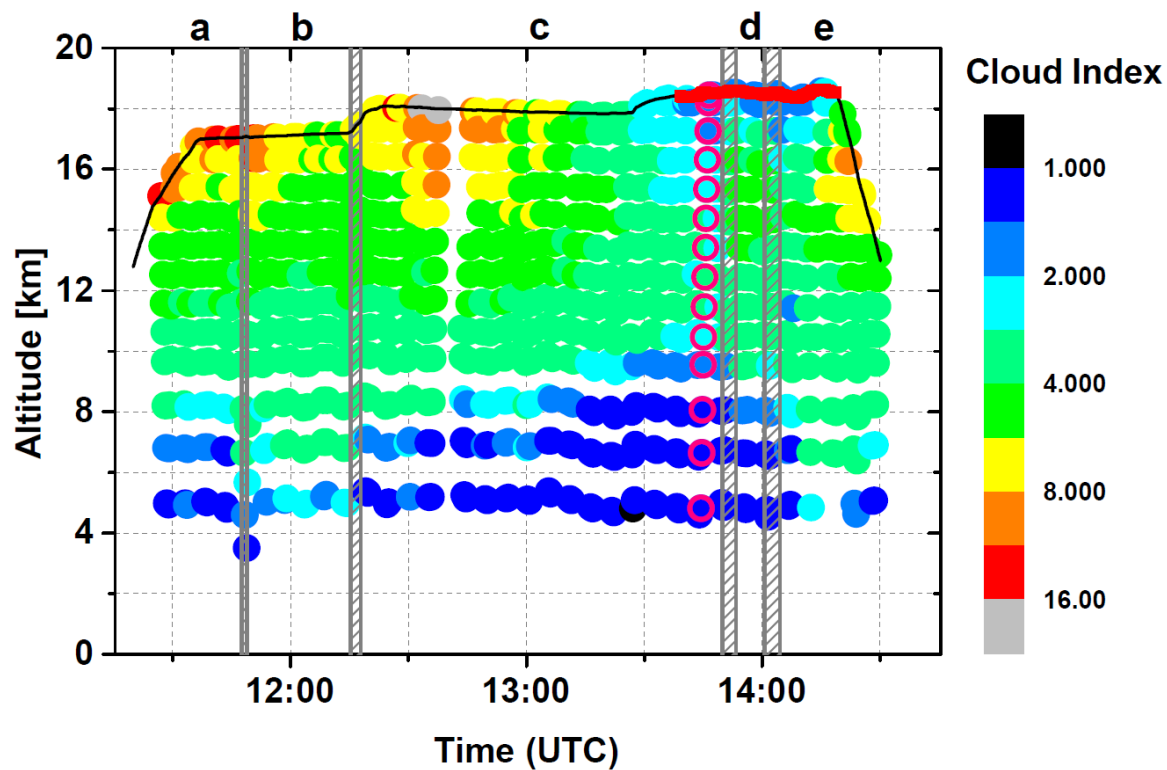
Figure 2. Vertical flight profile of the *Geophysica* (black line) and vertical distribution of the MIPAS-STR tangent points, colour-coded with the cloud index (filled circles). Open magenta circles: MIPAS-STR limb scan associated with spectra considered in radiative transfer simulations. Red line: flight section of FSSP-100 and CDP PSC observations. Grey hatched areas: turns between different legs.
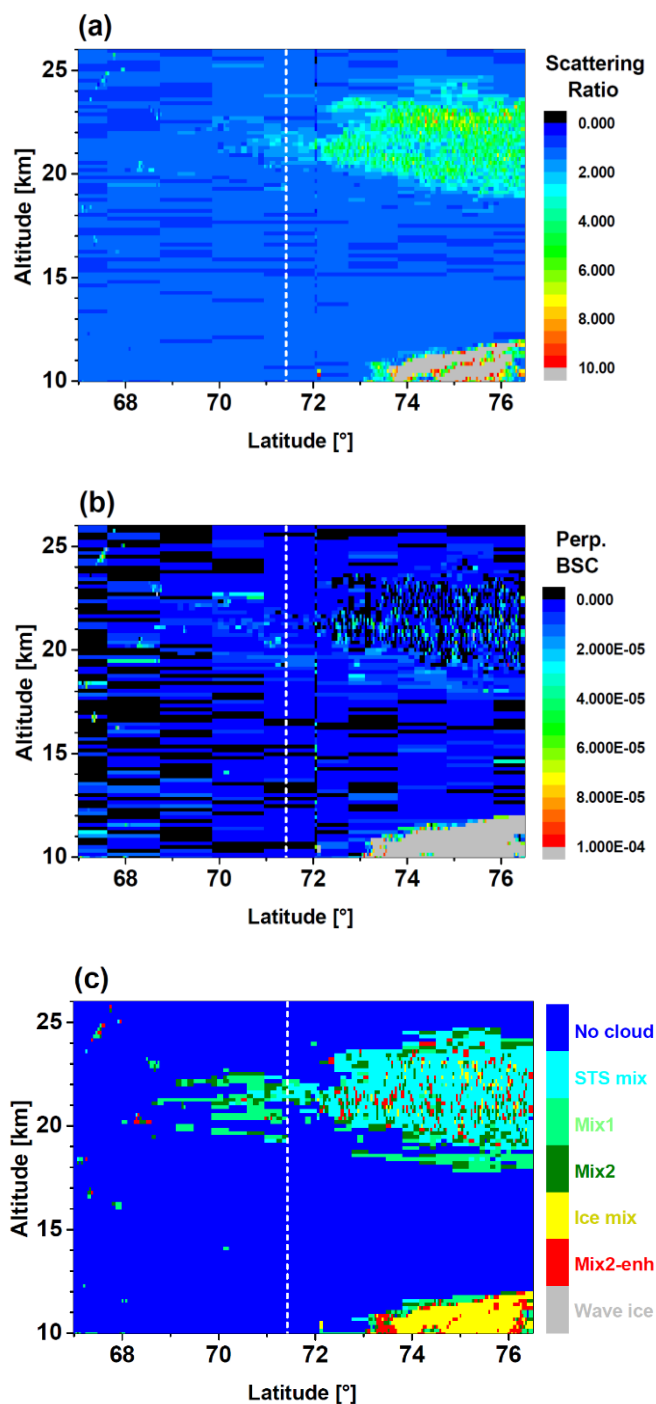
Figure 3. CALIPSO PSC observations associated with the *Geophysica* flight on 11 December 2011. **(a)** Scattering ratio at 532 nm. **(b)** Perpendicular backscatter (BSC) at 532 nm. **(c)** PSC classification according to Pitts et al. (2011, 2013). White dashed lines: latitude of northernmost observations aboard the *Geophysica*.
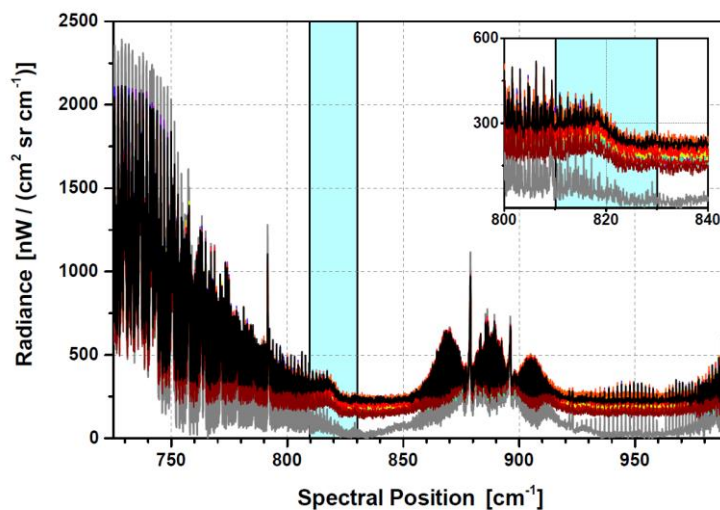
Figure 4a. MIPAS-STR channel 1 spectra of approximately horizontal limb views (~ -0.3° versus horizon). Coloured spectra: observations inside PSC in the time interval of the in-situ PSC observations. Black spectrum: PSC observation analysed in Sect. 3. Grey spectrum: Corresponding observation under cloud-free conditions. Spectral region of "shoulder-like" signature around 820 cm^{-1} attributed to β-NAT particles shaded in cyan.
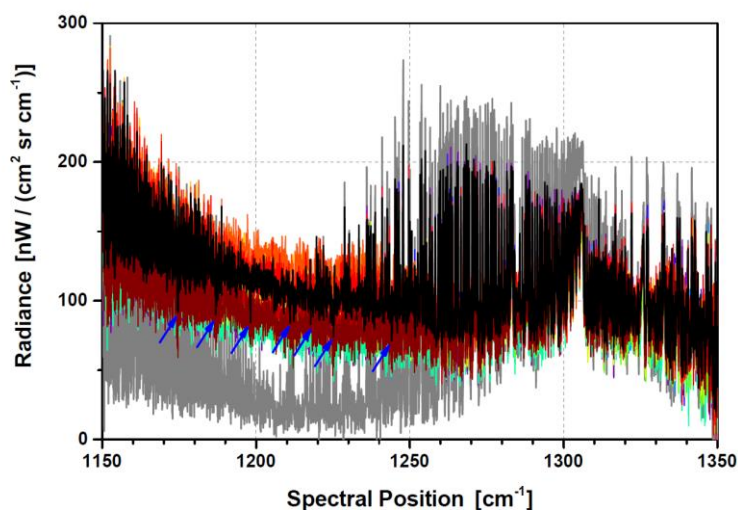
Figure 4b. Same as Figure 4a but for MIPAS-STR channel 2. Blue arrows denote prominent $H_2O_{(g)}$ absorption signatures from scattering of tropospheric radiation by PSC particles.
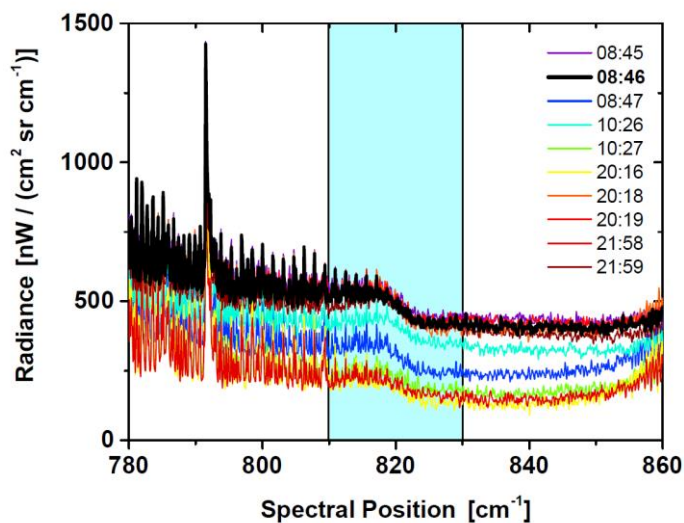
Figure 5. Spectral window of MIPAS-Envisat channel A observations with tangent altitudes between 18.4 and 19.0 km in the vicinity of the *Geophysica* flight on 11 December 2011. Geolocations are indicated in Figure 1. Observation times are given in UTC.
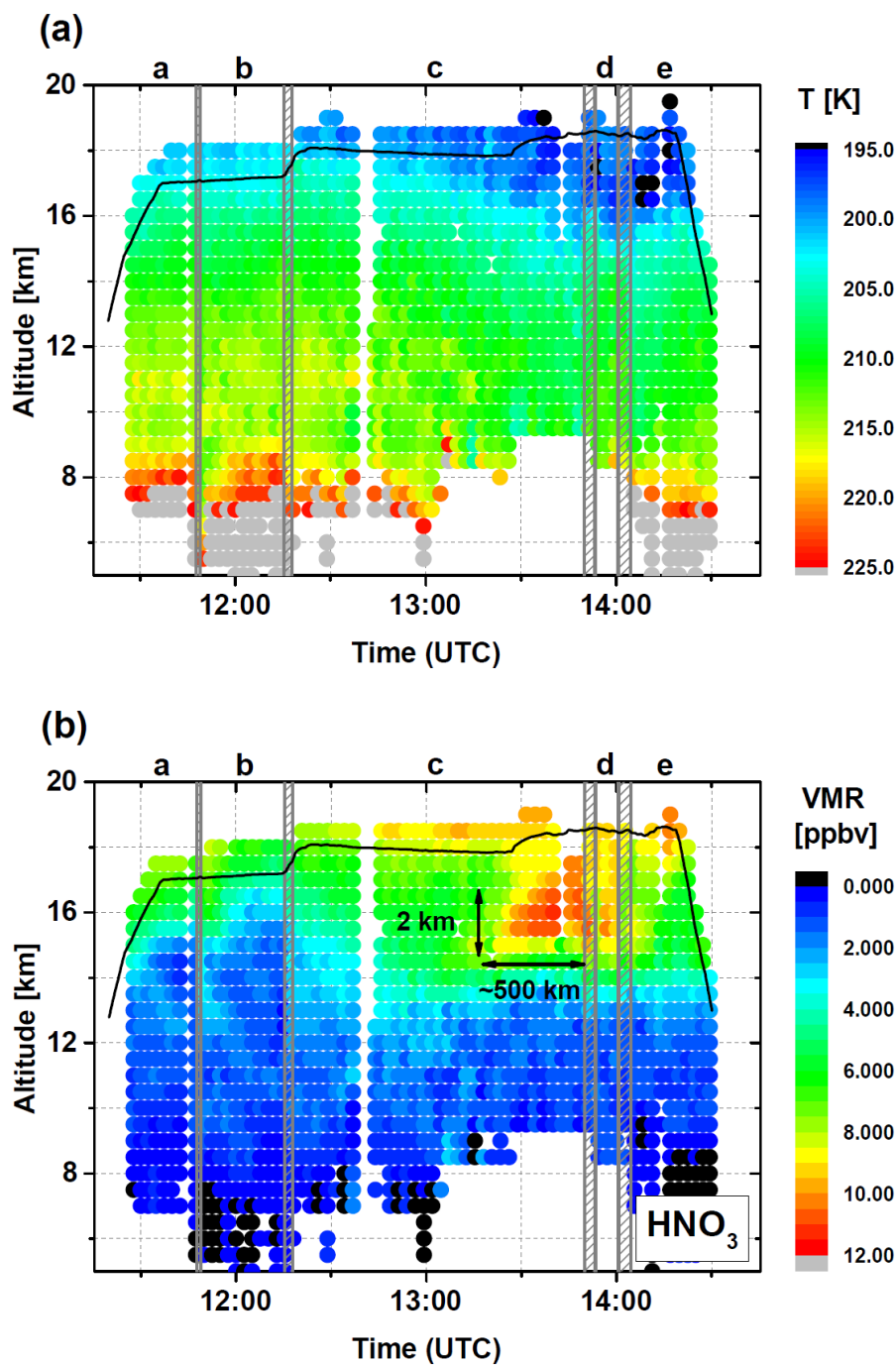
Figure 6. Vertical cross-sections of temperature (T) and $HNO_{3(g)}$ along flight track retrieved from the MIPAS-STR observations. Vertical flight profile (black line) and turns between different flight legs (grey hatched areas). Data points are filtered for a vertical resolution better than 5 km.
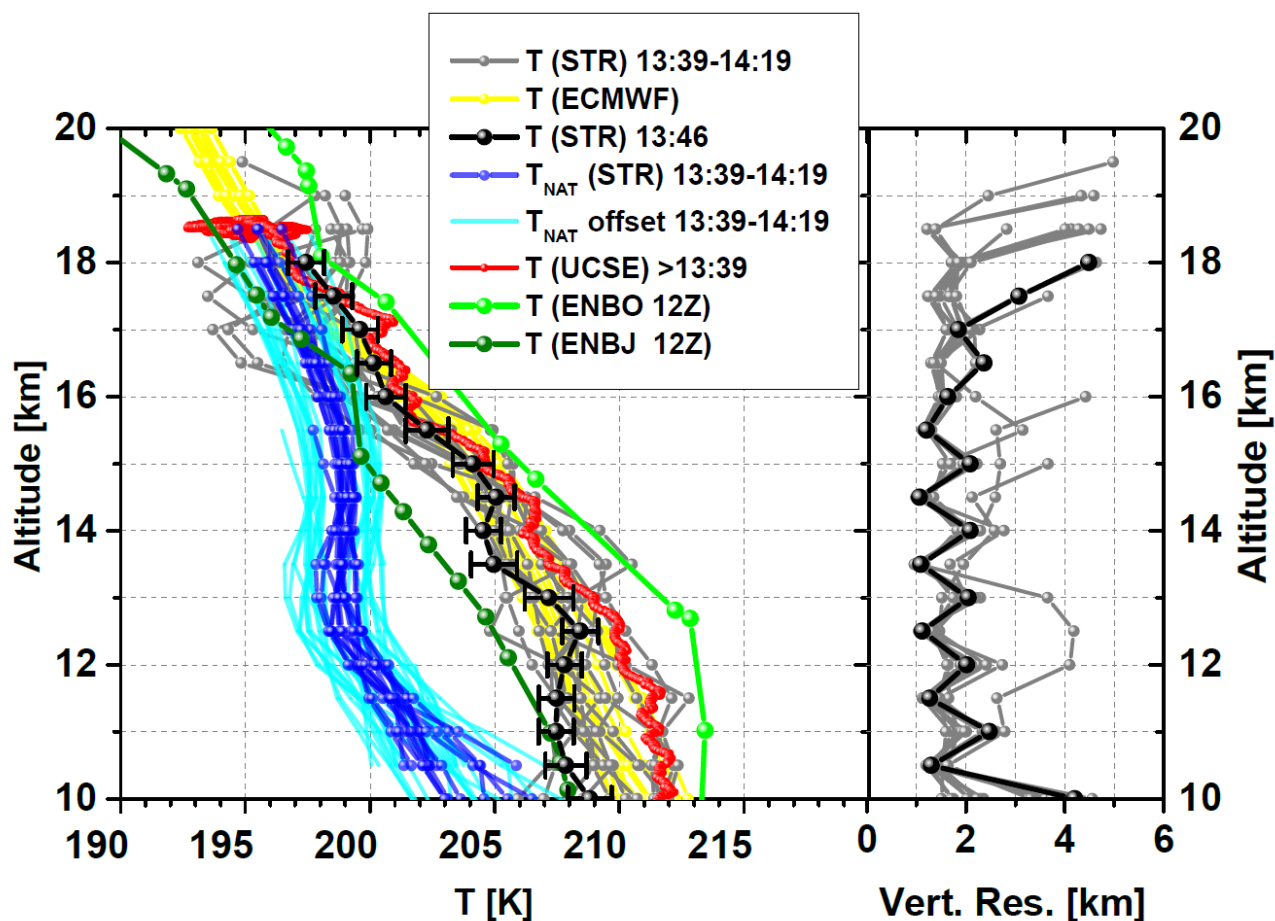
Figure 7. Left panel: MIPAS-STR temperature profiles (grey) associated with the *Geophysica* PSC encounter. Associated ECMWF initial guess/a priori profiles (yellow). Individual MIPAS-STR temperature profile (black) with combined random and systematic 1σ-uncertainties. In-situ measurements by the *Geophysica* UCSE onboard temperature sensor (red) during the PSC encounter and the subsequent descent phase. Radiosonde temperature profiles from Bodø (ENBO, green) and Bjornoya (ENBJ, dark green). T_{NAT} profiles calculated from the MIPAS-STR $HNO_{3(g)}$ and $H_2O_{(g)}$ profiles during the PSC encounter (blue) together with the same profiles (cyan) considering a simultaneous +20% and a simultaneous -20% offset for both species, respectively. Right panel: Vertical resolutions of MIPAS-STR profiles.
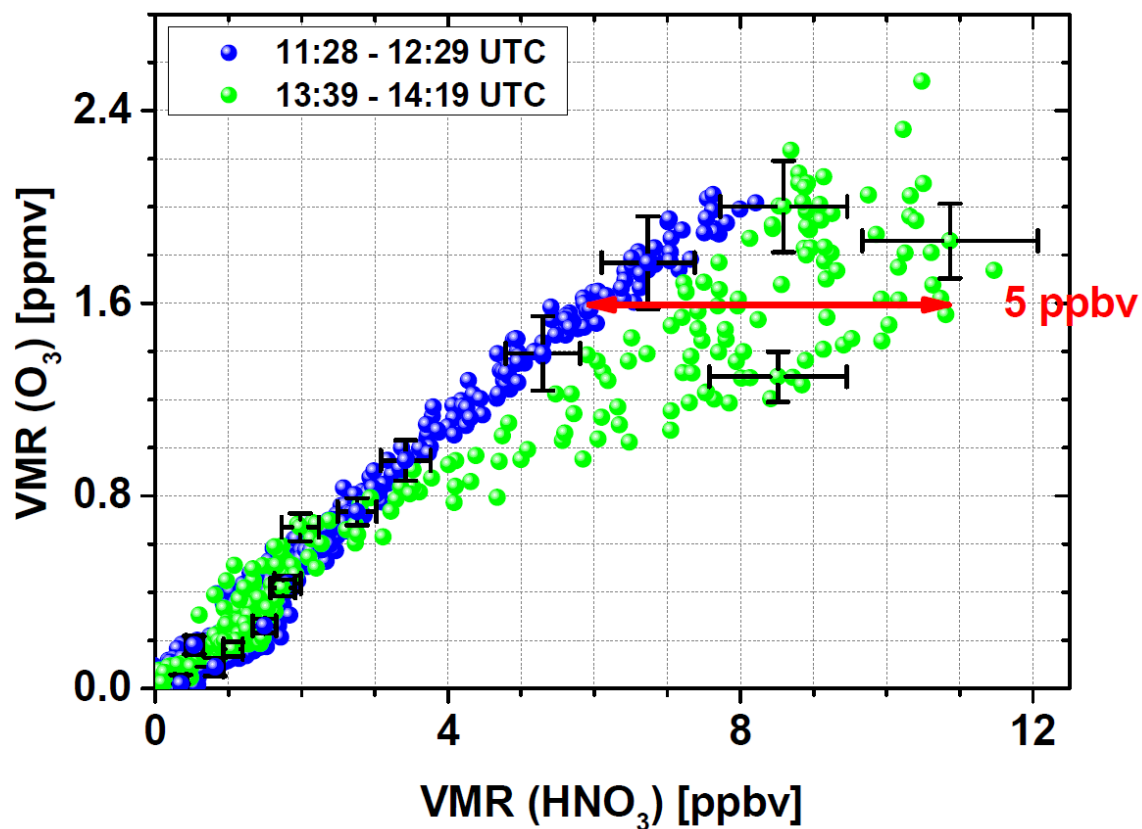
Figure 8. Correlation of O₃ with HNO₃(g) retrieved from the MIPAS-STR observations together with combined random and systematic 1σ-uncertainties of example data points.
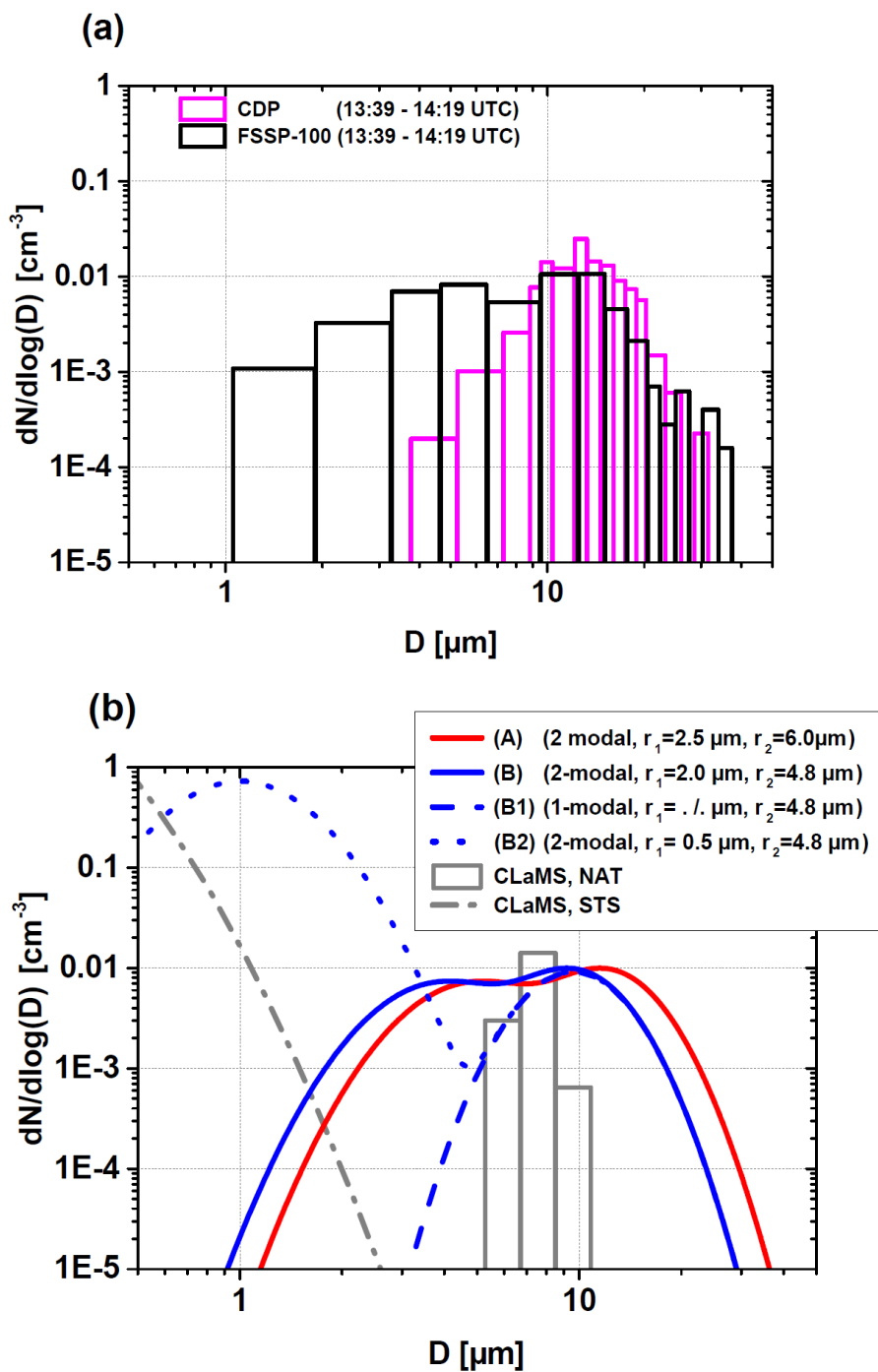
Figure 9. (a) Particle size distributions derived from the FSSP-100 (black) and CDP (magenta) measurements during the PSC encounter (from Molleker et al., 2014, Fig. 12). (b) Particle size distributions used in radiative transfer simulations of MIPAS-STR PSC spectra (red and blue) and simulated by the CLaMS (grey). Note that particle sizes are indicated in diameter (D).
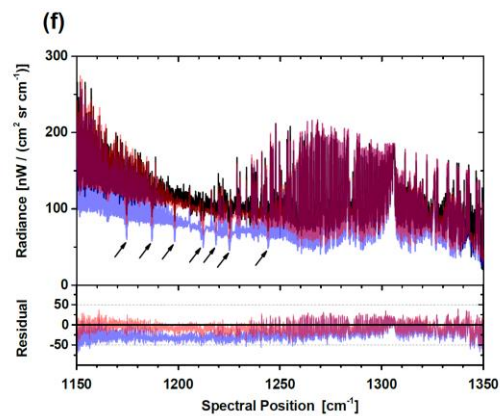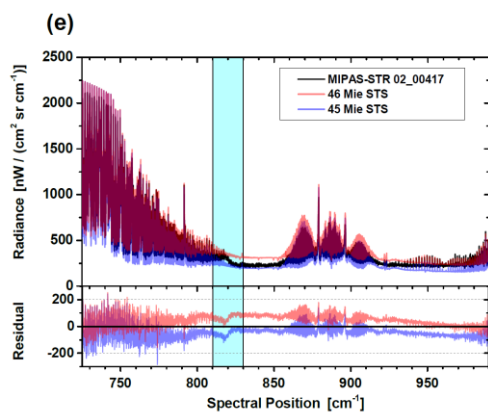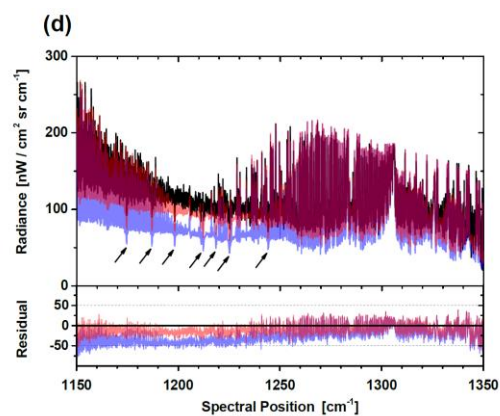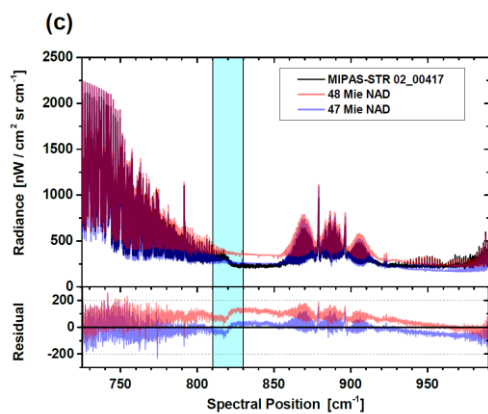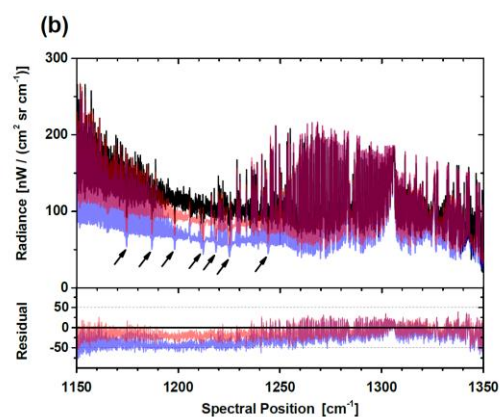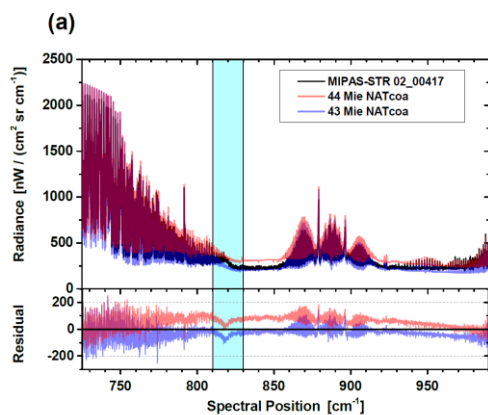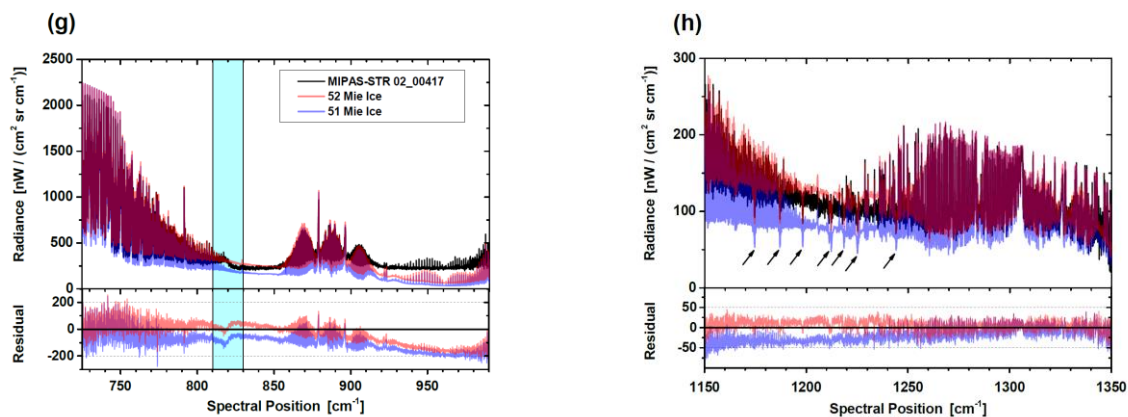
Figure 10. Mie calculations for spherical particles. Black spectra in all panels: MIPAS-STR limb observation (13:47 UTC, tangent altitude 18.4 km). Simulations of (a) and (b) β-NAT, (c) and (d) NAD, (e) and (f) STS, and (g) and (h) ice with size distributions A (red) and B (blue). Lower panels: residuals between the simulations and the observation. Black arrows denote prominent H_2O absorption signatures from scattering of tropospheric radiation by PSC particles. Numbers in legend refer to scenarios in Table 1.
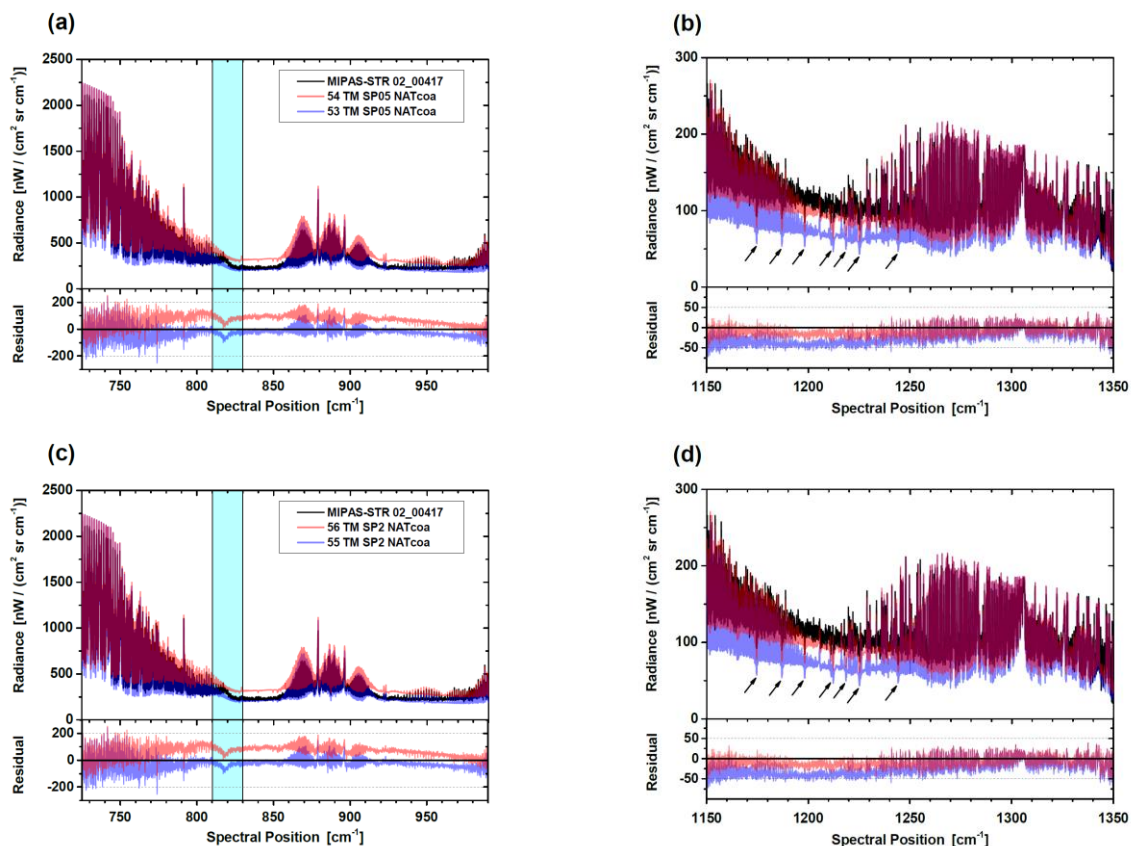
Figure 11. T-Matrix calculations for moderately aspherical β-NAT particles. Black spectra in all panels: MIPAS-STR limb observation (13:47 UTC, tangent altitude 18.4 km). Simulations of β-NAT with (a) and (b) AR=0.5, and (c) and (d) AR=2.0 with size distributions A (red) and B (blue). Lower panels: residuals between the simulations and the observation. Black arrows denote prominent H_2O absorption signatures from scattering of tropospheric radiation by PSC particles. Numbers in legend refer to scenarios in Table 1.
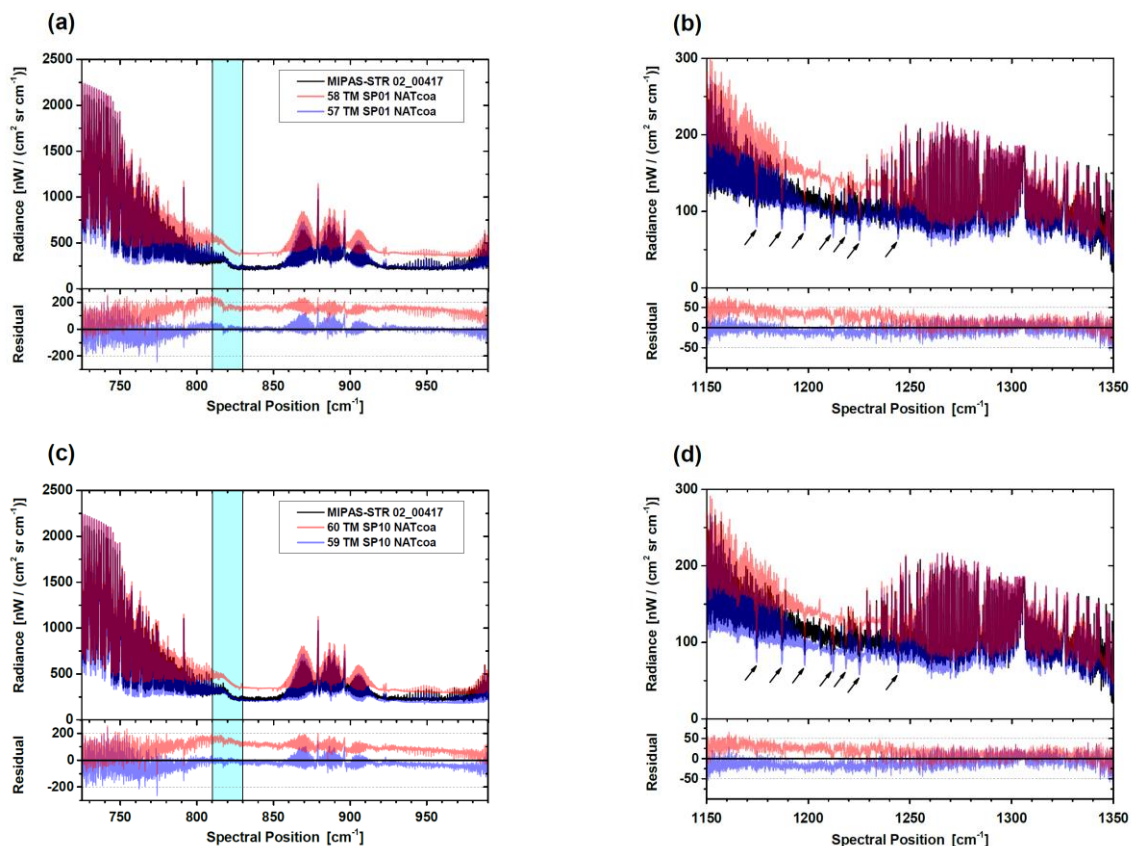
Figure 12. T-Matrix calculations for highly aspherical β-NAT particles. Black spectra in all panels: MIPAS-STR limb observation (13:47 UTC, tangent altitude 18.4 km). Simulations of β-NAT with (a) and (b) AR=0.1, and (c) and (d) AR=10.0 with size distributions A (red) and B (blue). Lower panels: residuals between the simulations and the observation. Black arrows denote prominent H_2O absorption signatures from scattering of tropospheric radiation by PSC particles. Numbers in legend refer to scenarios in Table 1.
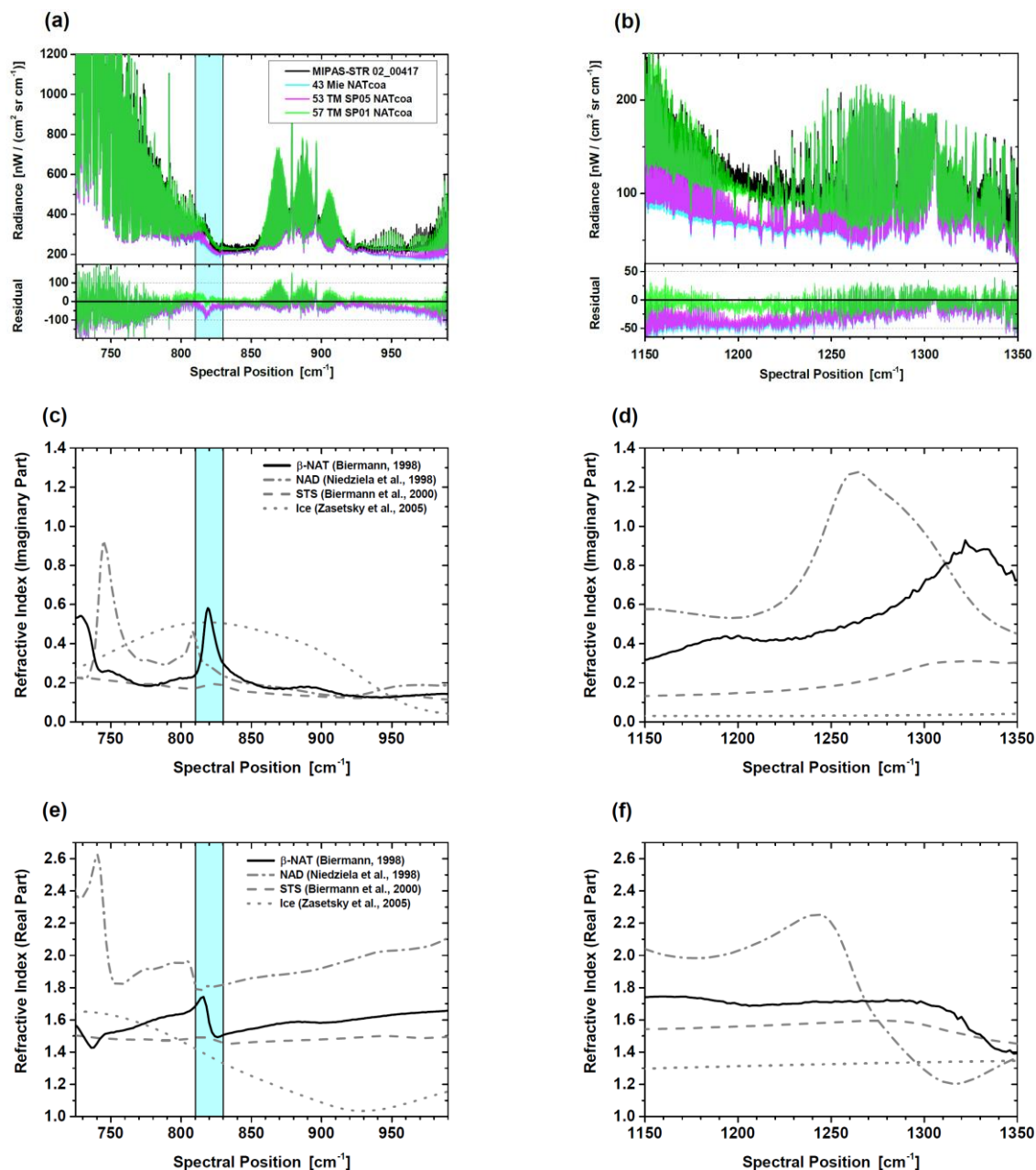
Figure 13. Dependence of simulated spectral signatures of β-NAT particles on degree of non-sphericity. (a) and (b): Black: MIPAS-STR limb observation (13:47 UTC, tangent altitude 18.4 km). Mie calculation for spherical particles (cyan), T-Matrix calculation with AR=0.5 (magenta) and T-Matrix calculation with AR=0.1 (green). Lower panels: residuals between the simulations and the observation. Numbers in legend refer to scenarios in Table 1. Refractive index (c) and (d) imaginary and (e) and (f) real parts of β-NAT, NAD, STS and ice.
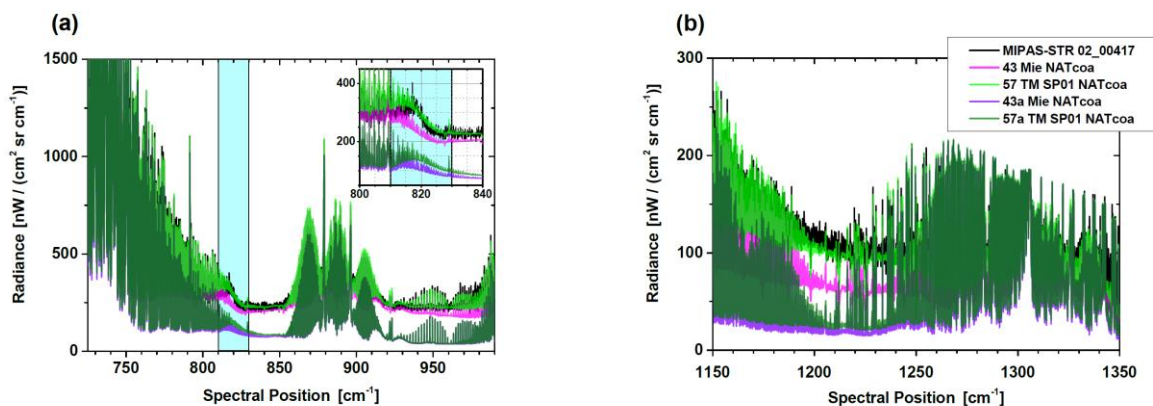
Figure 14. Relative roles of emission and scattering by spherical particles and highly elongated spheroids consisting of β-NAT. Black: MIPAS-STR limb observation (13:47 UTC, tangent altitude 18.4 km). Magenta/violet: simulations of spherical particles (AR=1.0) with/without scattering. Green/dark green: simulations of highly elongated particles (AR=0.1) with/without scattering. Numbers in legend refer to scenarios in Table 1.
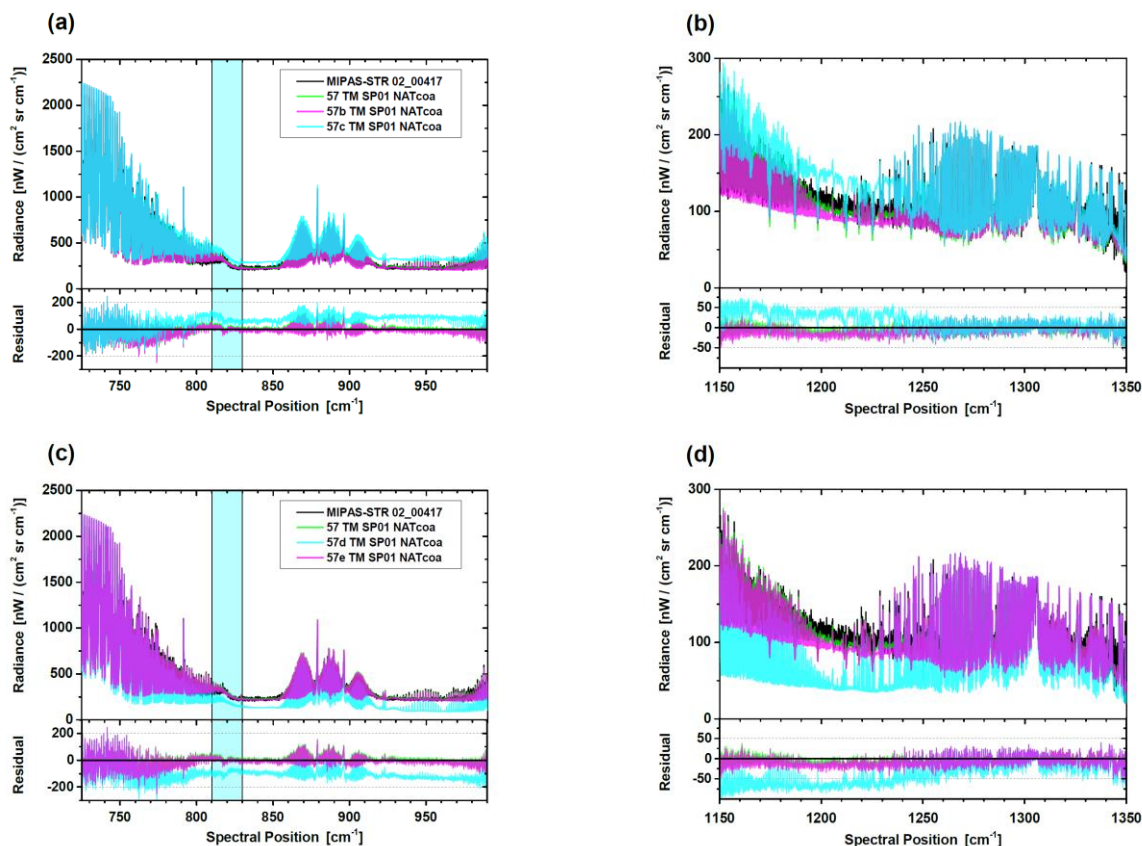
Figure 15. Influence of tropospheric scenario on simulations of elongated spheroids with AR=0.1 consisting of β-NAT. Black spectra in all panels: MIPAS-STR limb observation (13:47 UTC, tangent altitude 18.4 km). Green spectra in all panels (mostly hidden by magenta spectra): optimized scenario. (a) and (b): sensitivity simulations assuming an opaque tropospheric cloud between 0 and 2 km (magenta) and the absence of any tropospheric cloud (cyan). (c) and (d): sensitivity simulations assuming an opaque tropospheric cloud from 0 to 10 km (cyan) and a surface temperature reduced by 7 K (magenta). Numbers in legend refer to scenarios in Table 1.
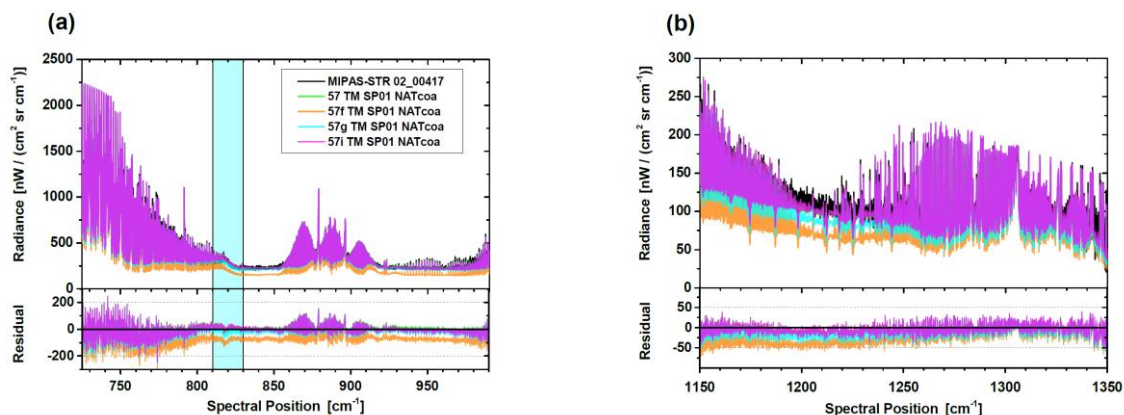
Figure 16. Influence of PSC layer thickness and particle size distribution on simulations of elongated spheroids with AR=0.1 consisting of β-NAT. Black: MIPAS-STR limb observation (13:47 UTC, tangent altitude 18.4 km). Green (mostly hidden by magenta spectra): optimized scenario (assuming a vertical extent of the PSC from 17 to 23 km and size distribution B). Orange: sensitivity simulation assuming a reduced vertical extent of the PSC from 17 to 20 km. Cyan and magenta: sensitivity simulations using size distributions B1 and B2. Numbers in legend refer to scenarios in Table 1. For size distributions see Table 2 and Figure 9b.
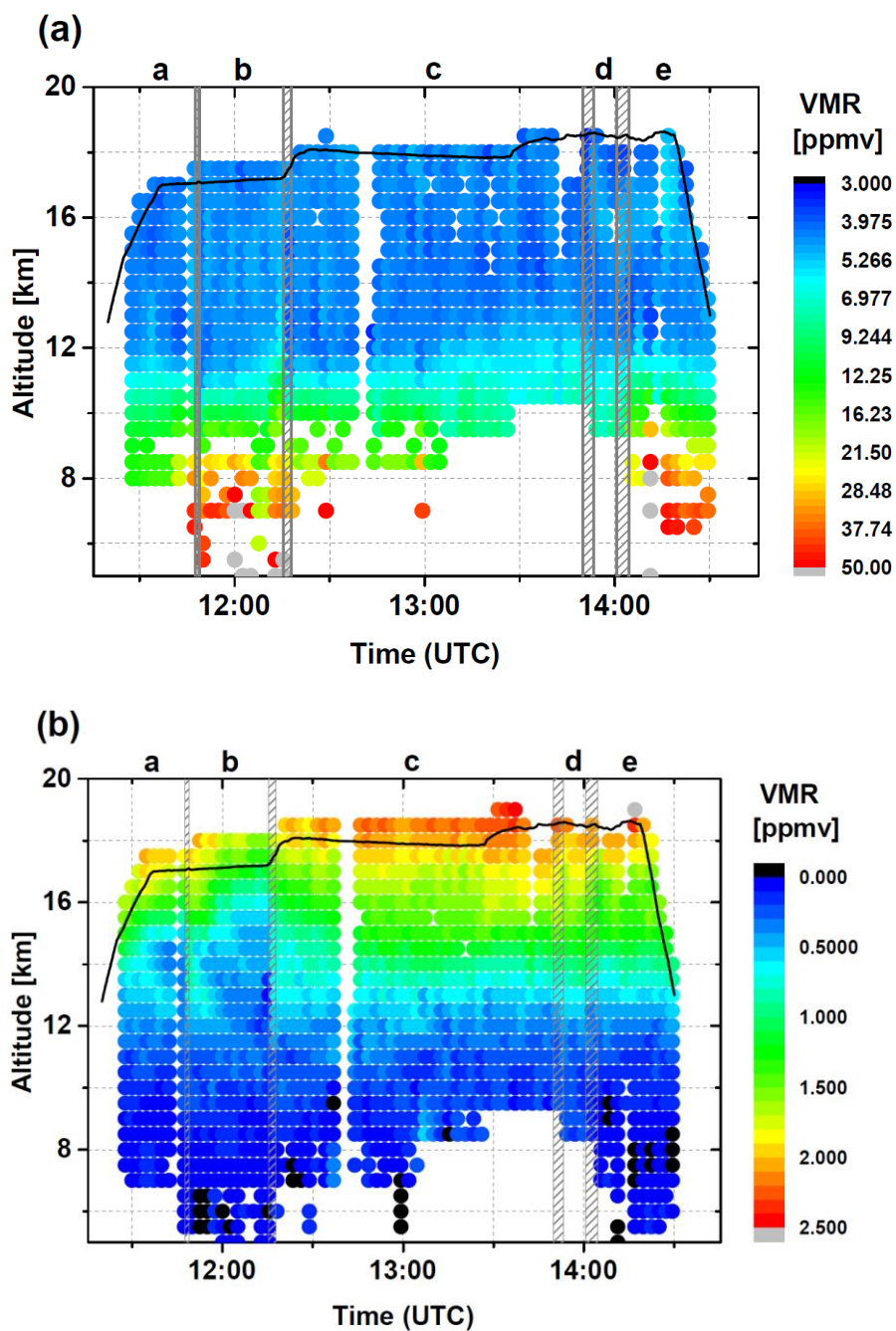
Figure 17. Vertical cross-sections of $H_2O_{(g)}$ and O_3 along flight track retrieved from the MIPAS-STR observations. Vertical flight profile (black line) and turns between different flight legs (grey hatched areas). Data points are filtered for a vertical resolution better than 5 km.
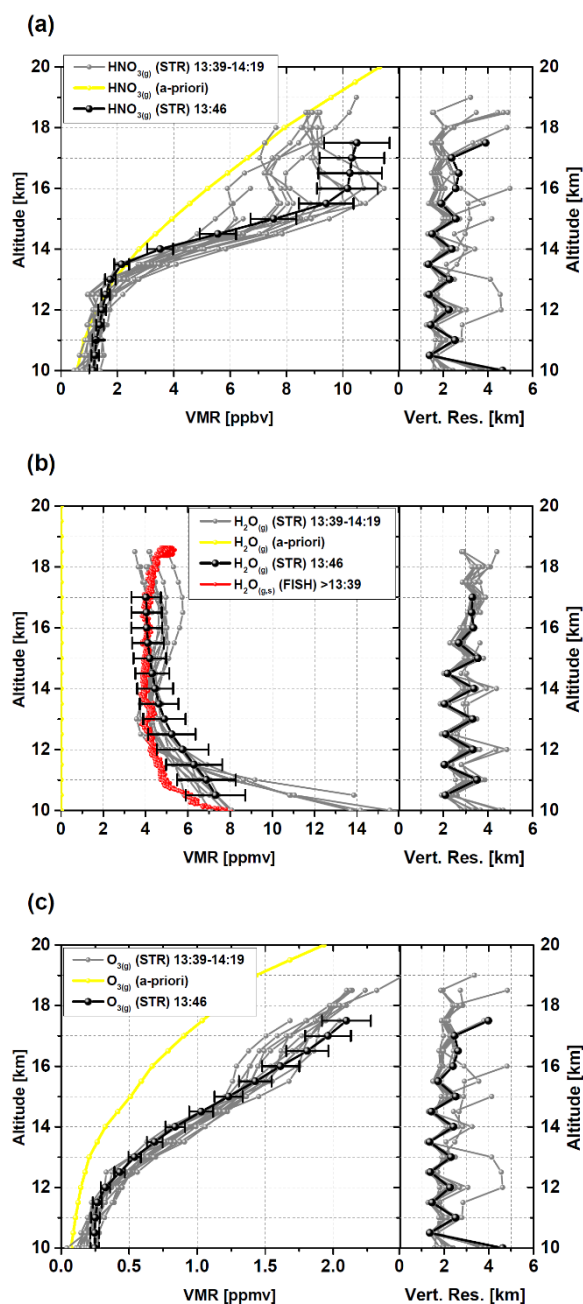
Figure 18. Left panels: Vertical profiles of $HNO_{3(g)}$, $H_2O_{(g)}$ and O_3 retrieved from the MIPAS-STR observations during the PSC encounter (grey and black) including initial guess/a priori profiles (yellow; $HNO_{3(g)}$ and O_3: Remedios et al., 2007; $H_2O_{(g)}$: 0 ppmv at all altitudes). For H_2O, collocated FISH total $H_2O_{(g+s)}$ measurements during the PSC encounter and the subsequent descent phase are shown for comparison. Right panels: Vertical resolutions of MIPAS-STR profiles.